Selective abrogation of S6K2 maps lipid homeostasis as a survival vulnerability in MAPKi-resistant NRAS^{MUT} melanoma

Hsin-Yi Chen[1], Aaron R. Goldman[1,5], Delaine Zayas-Bazan[6], Patricia I. Reyes-Uribe[1], Adam N. Guterres[1], Brittany Lipchick[1], Subhasree Basu[1], Xiangfan Yin[1], Mark J. Axelrod[3], Yiling Lu[4], Zachary Schug[1], Andrew V. Kossenkov[1], Gordon B. Mills [4&], Qin Liu[1], Michael J. Weber[3*], Maureen E. Murphy[1,2], David W. Speicher[1,2] & Jessie Villanueva[1,2,7**]

[1] Molecular & Cellular Oncogenesis Program, The Wistar Institute, Philadelphia, PA 19104, USA
[2] Melanoma Research Center, The Wistar Institute, Philadelphia, PA 19104, USA
[3] Department of Microbiology, Immunology, and Cancer Biology, University of Virginia, Charlottesville, VA 22908, USA
[4] Department of Systems Biology, The University of Texas MD Anderson Cancer Center, Houston, TX 77030, USA
[5] The Proteomics and Metabolomics Core Facility, The Wistar Institute, Philadelphia, PA 19104 USA
[6] Biochemistry and Molecular Biophysics Graduate Group, Perlman School of Medicine, University of Pennsylvania, Philadelphia, PA 19104, USA
[7] Lead Contact
[&] Current Affiliation: OHSU Knight Cancer Institute, Portland, OR 97239, USA

***** This paper is dedicated to the memory of Michael J. Weber

****Correspondence:** jvillanueva@wistar.org

RUNNING TITTLE: S6K2 is a vulnerability in MAPKi-resistant NRAS-mutant melanoma

SUMMARY

Although oncogenic NRAS activates MAPK signaling, inhibition of the MAPK pathway is not therapeutically efficacious in NRAS-mutant tumors. Here we report that silencing the ribosomal protein S6 kinase 2 (S6K2), while preserving the activity of S6K1, perturbs lipid metabolism, enhances fatty acid unsaturation, triggers lipid peroxidation and induces cell death selectively in NRAS-mutant melanoma cells that are resistant to MAPK inhibition. S6K2 depletion stimulates SREBP1 activity in an S6K1-dependent manner and relieves suppression of PPARα, triggering apoptosis and ferroptosis. Combining PPARα agonists and polyunsaturated fatty acids phenocopies the effects of S6K2 abrogation, blocking tumor growth. Collectively, our study establishes S6K2 and its effector subnetwork as promising targets for NRAS-mutant melanoma that are resistant to global MAPK pathway inhibitors.

Key Words:

MAPKi-resistance, mutant NRAS, melanoma, S6K2, PPARα, lipid desaturation, lipid peroxidation, oxidative cell death

INTRODUCTION

RAS-mutant tumors are highly aggressive and mostly refractory to currently available targeted therapies. In cutaneous melanoma, mutations in NRAS account for almost 30% of all tumors (Hayward et al., 2017). Oncogenic NRAS elicits persistent activation of the RAF/MEK/ERK (MAPK) cascade, which plays a key role in melanomagenesis; therefore, inhibition of MAPK has been evaluated as a potential therapeutic approach for NRAS-mutant melanoma. However, inhibitors of the MAPK pathway as single agents elicit less than 20% response rate and do not prolong the survival of NRAS-mutant melanoma patients compared to chemotherapy (Dummer et al., 2017; Sullivan et al., 2018). Further, suppression of MAPK signaling often leads to feedback or compensatory activation of PI3K/AKT, another RAS effector pathway governing cell growth and survival in melanoma (Atefi et al., 2011; Fattore et al., 2013; Gopal et al., 2010; Vu and Aplin, 2016). Yet, drug combinations that inhibit both the MAPK and PI3K pathways are poorly tolerated in patients, and clinically efficacious doses have not been achieved (Eroglu et al., 2019; Juric et al., 2014; Posch et al., 2016; Tolcher et al., 2015). Although simultaneous inhibition of the MAPK and PI3K pathways is generally toxic, there is no evidence that the proximal molecular causes of that toxicity are the same in normal and in cancer tissues. This raises the possibility that targeting a convergent subnetwork or node, downstream from the PI3K and MAPK pathways, could elicit lethality in melanoma cells, while sparing normal tissues. Thus, mapping out the downstream subnetwork could help identify much needed actionable drug targets for NRAS-mutant tumors.

Dual inhibition of MEK and PI3K in NRAS-mutant melanoma pre-clinical models led to substantial perturbation of metabolic pathways (Posch et al., 2013). The mechanistic target of rapamycin protein complex 1, mTORC1, is a critical regulator of metabolism that acts as a signaling hub downstream of RAS (Duvel et al., 2010), integrating upstream signals, including the MAPK and PI3K pathways (Corcoran et al., 2013; Magnuson et al., 2012). Key effectors of mTORC1 are the 40S ribosomal kinases (S6K), S6K1 and S6K2 (Sridharan and Basu, 2020b). The S6K pathway plays important roles in gene transcription, protein translation, cellular metabolism and cell survival (Magnuson et al., 2012; Pardo and Seckl, 2013; Sridharan and Basu, 2020a). Despite the high degree of structural homology between S6K1 and S6K2, their expression, activation and cellular localization are differentially regulated (Sridharan and Basu, 2020b). Notably, loss of S6K1 leads to compensatory upregulation of S6K2 and vice versa (Nardella et al., 2011; Pende et al., 2004; Shima et al., 1998). Further, S6K1 and S6K2 have overlapping, as well as distinct or even opposite biological functions (Karlsson et al., 2015; Magnuson et al., 2012; Nardella et al., 2011; Pardo and Seckl, 2013; Pavan et al., 2016; Sridharan and Basu, 2020b). This suggests that the functional activity of these two kinases should be tightly coordinated and imbalance between these two kinases could lead to differential outcomes.

Here, we identified a S6K1/S6K2/SREBP/PPARα subnetwork downstream of the MAPK and PI3K pathways. Perturbation of this subnetwork by uncoupling S6K1 and S6K2 triggers a lipid metabolic imbalance, leading to oxidative cell death selectively in NRAS-mutant melanomas that are resistant to MAPK inhibition. Further, we provide proof-of-concept that this vulnerability can be exploited to curb MAPKi-resistant tumors and to inform the design of future strategies to combat NRAS-mutant melanoma.

RESULTS

S6K2 is a vulnerability in NRAS-mutant melanoma resistant to MAPK inhibitors

MAPK inhibition elicits heterogeneous effects in NRAS-mutant melanoma (Ascierto et al., 2013). Therefore, we sought to identify potential vulnerabilities in MAPK inhibitor (MAPKi)-resistant tumor cells. To this end, we analyzed the effect of MEK or ERK inhibitors on proliferation and cell death in NRAS-mutant melanoma cells (Figures S1A-C, Table S1). MAPKi induced variable effects (Figures S1A-C), despite effective and persistent inhibition of the MAPK pathway (Figures S1D-E). We classified cells as MAPKi-resistant or MAPKi-sensitive based on their response to MAPKi, defined as area under the curve (AUC) (for resistant cells, MEKi/trametinib: AUC>2.4; ERKi/ SCH772984: AUC>2.3), as well as suppression of cell proliferation and induction of cell death (Figure S1A-C). MAPKi elicited modest suppression of proliferation (Figure S1B) and marginal induction of cell death (Figure S1C) in the MAPKi-resistant cells. This heterogeneous response to MAPKi was further validated in a larger panel of NRAS-mutant melanoma cells (Table S1) treated with two additional clinically relevant MAPKi (MEKi: MEK-162 and ERKi: BVD-523; Figure S1F).

We noted that resistance to MAPK inhibition was associated with low basal levels of pERK (Pearson's correlation $|R|>0.5$, $P<0.05$) (Figures S1G and H), suggesting that MAPKi-resistant cells have relatively low input to ERK and potentially less dependence on ERK signaling. To further explore the signaling networks in MAPKi-resistant *vs.* MAPKi-sensitive cells, we first performed biochemical analysis of cells treated with either the MEK inhibitor trametinib (Tram) or the ERK inhibitor SCH772984 (SCH984), collectively referred to as MAPKi. MAPKi suppressed the MAPK pathway to similar levels in both sensitive and resistant cells (Figures 1A and S1D and Table S2). The PI3K/AKT pathway was similarly activated in all MAPKi-treated cell lines (Figures 1A and S1D and Table S2). In contrast,

MAPKi treatment blocked phosphorylation of S6 kinase (S6K) and its substrate S6 in MAPKi-sensitive, but not in MAPKi-resistant melanoma cells (Figures 1A and S1D and Table S2).

Since S6K is also a bona fide effector of the PI3K/mTOR pathway (Lee-Fruman et al., 1999), we assessed whether S6K is regulated by this pathway in NRAS-mutant melanoma cells. PI3K/mTOR inhibitors suppressed phosphorylation of S6 (pS6) in both MAPKi-resistant and MAPKi -sensitive NRAS-mutant melanoma cells (Figures S1I and J). To further examine the impact of MAPK or PI3K/mTOR signaling on S6K, we ectopically expressed constitutively active S6K (S6K1E389 or S6K2E388) constructs in MAPKi-sensitive or resistant cells (Figures 1B and S1K) and assessed levels of $pS6^{S240/244}$, a site exclusively phosphorylated by S6K (Corcoran et al., 2013; Meyuhas, 2008; Roux et al., 2007). Treatment of MAPKi-sensitive cells with MAPKi (SCH984) or PI3K/mTORi (GSK458) decreased phosphorylation of S6; ectopic expression of S6K1E389 or S6K2E388 rescued pS6 levels in cells treated with SCH984 or GSK458. These data indicate that S6K mediates both MAPK and PI3K/mTOR signaling in MAPKi-sensitive cells (Figures 1B and S1K). In contrast, in MAPKi-resistant cells, treatment with MAPKi had no effect on phosphorylation of S6, whereas treatment with PI3K/mTORi effectively suppressed pS6 (Figures 1B and S1K). Ectopic expression of S6K1E389 or S6K2E388 rescued pS6 levels in MAPKi-resistant cells treated with PI3K/mTORi (Figures 1B and S1K). Together, these data indicate that S6K activity is regulated by the PI3K/mTOR pathway in MAPKi-resistant cells. Further, these findings highlight that different upstream pathways differentially impinge on S6 kinase in MAPKi-resistant *vs.* MAPKi-sensitive cells (Figure 1C).

To assess the role of S6K in NRAS-mutant melanoma cells, we silenced S6K1 or S6K2 in six (3 sensitive and 3 resistant to MAPKi) NRAS-mutant melanoma lines. Depletion

of either S6K1 or S6K2 impaired cell proliferation in all cell lines tested (Figures S1L and M). Depletion of S6K2, but not S6K1, induced cell death in MAPKi resistant cells (Figures 1D, 1E and S1N). Neither depletion of S6K1 nor S6K2 triggered substantial cell death in MAPKi-sensitive NRAS-mutant melanoma cells (Figures 1F and S1O) or non-transformed human fibroblasts (Figure S1P). These data point to S6K2 as a vulnerability selectively in NRAS-mutant melanoma cells that are resistant to MAPKi (Figure 1G).

We also examined data from melanoma patients in the TCGA skin cutaneous melanoma dataset (N=470). We noted that S6K2 mRNA levels were inversely correlated with S6K1 (R=-0.462, p val=3.15 e-26 Fig. 1H). We then assessed whether S6K1 or S6K2 levels were associated with patient survival. In patients who had received targeted therapies as one of their treatments (n=355), low expression of S6K2 was associated with better patient survival (p= 0.013; Fig. 1I, right panel). In contrast, S6K1 levels were not significantly associated with patient survival (Fig, 1I, left panel). These data further support the notion that S6K2 could have an important role in melanoma and may constitute a vulnerability in this tumor type.

Depletion of S6K2 triggers lipid peroxidation facilitating cell death

To investigate the mechanism(s) whereby S6K2 depletion triggers cell death in MAPKi-resistant cells, we surveyed the proteome to identify proteins that were differentially affected by depletion of S6K2 versus S6K1 in MAPKi-resistant cells. Depletion of S6K2 was coupled to enhanced expression of proteins involved in lipid synthesis, fatty acid synthesis, uptake and activation, and phospholipid remodeling (Figures 2A, S2A and S2B, and Tables S2 and S3). To further assess if lipid metabolism was perturbed by S6K2 depletion, we performed unbiased global lipidomic analysis in S6K2 or S6K1-depleted cells. S6K2 depletion was associated with significantly increased levels of triacylglycerols

(Figure S2C and Table S4), consistent with disrupted lipid homeostasis. Notably, compared to S6K1 depletion, depletion of S6K2 led to an enrichment of specific lipid species containing polyunsaturated fatty acyl chains (PUFA) such as phosphatidylcholine, phosphatidylethanolamine, phosphatidylglycerol and triacylglycerols (Figures 2B, S2C and S2D). These results suggest that S6K2 blockade is coupled to an enhanced degree of fatty acid unsaturation in some lipid classes. We also noted that depletion of S6K1 or S6K2 led to increased levels of proteins involved in oxidative stress response, including ROS sensing/detoxifying enzymes such as SOD2 and PARK7 (Figures 2A, S2A and S2B and Tables S2 and S3). Accordingly, depletion of either S6K1 or S6K2 led to increased ROS levels (Figure 2C).

The effects of S6K2 depletion perturbing redox balance and lipid homeostasis raised the possibility that S6K2 depletion could be triggering cell death by inducing lipid peroxidation (Ayala et al., 2014). Accordingly, depletion of S6K2 but not S6K1 substantially enhanced lipid peroxidation, as indicated by the lipid ROS sensor Bodipy-C11 and generation of 4-HNE adducts (Figures 2D, S2E-G). S6K2 depletion also led to increased levels of nucleic acid oxidative damage (8-OHdG) and DNA double-strand breaks (p-γH2AX and 53BP1) (Figures S2H-K). Additionally, the ROS scavenger NAC, or the lipid ROS scavenger trolox (Barclay et al., 1995), attenuated cell death triggered by S6K2 depletion (Figures 2E and F), indicating that ROS contributes to cell death triggered by S6K2 depletion. Notably, S6K2 depletion induced lipid ROS preferentially in MAPKi-resistant cells, further supporting a role of lipid peroxidation in mediating S6K2sh-triggered cell death (Figures 2G, S2L). Together, these results support the premise that depletion of S6K2 enhances lipid metabolism and ROS levels, which jointly trigger lethal lipid peroxidation and oxidative cell death in MAPKi-resistant NRAS-mutant melanoma.

Excessive lipid peroxidation has been linked to different types of cell death including necrosis, apoptosis, and necroptosis (Aitken et al., 2012; Ayala et al., 2014; Canli et al., 2016; Seiler et al., 2008). Likewise, availability of PUFA-containing phospholipids and accumulation of lipid peroxides is linked to ferroptosis, an iron-dependent form of regulated cell death (Dixon et al., 2012; Magtanong et al., 2016; Yang et al., 2014). Our proteomic analysis indicated that S6K2 depletion enhanced pathways associated with ferroptosis (e.g. squalene metabolism, phospholipid remodeling and arachidonic acid metabolism) (Friedmann Angeli et al., 2014; Magtanong et al., 2016; Shimada et al., 2016; Viswanathan et al., 2017) (Figures 2A and S2A). Accordingly, S6K2-depleted cells showed increased levels of the ferroptosis marker PTGS2 (Figure S2M). We therefore examined whether S6K2 depletion could be triggering a ferroptosis-like form of cell death. Treatment of NRAS-mutant melanoma cells with the ferroptosis/lipid peroxidation inhibitors ferrostatin-1 (Fer-1) (Skouta et al., 2014) or liproxstatin-1 (Lip-1) (Friedmann Angeli et al., 2014; Kagan et al., 2017) or the iron chelator deferoxamine (DFO), attenuated cell death triggered by S6K2 depletion (Figure S2N-O). Since caspase-3 cleavage was also detected in S6K2-depleted cells (Figure 1E), we asked if depletion of S6K2 could be triggering other forms of cell death. Treatment of S6K2-depleted cells with inhibitors of apoptosis (zVAD) or ferroptosis (Fer-1) partially restored viability of S6K2-depleted cells, whereas the necroptosis inhibitor (necrostatin-1; Nec-1) did not prevent cell death (Figure 2H). Together, these results suggest that S6K2 depletion triggers both apoptosis and ferroptosis-like cell death.

S6K1 and SREBP contribute to oxidative cell death

To identify S6K2 effectors that could trigger cytotoxicity, we next dissected the S6K2 downstream signaling subnetwork by assessing the transcriptional changes triggered by S6K2 depletion. In cells expressing S6K2 shRNA, target genes of master lipid homeostasis

regulators, Sterol regulatory element-binding proteins (SREBPs) and Peroxisome proliferator-activated receptors (PPARs), were overrepresented, suggesting that suppression of S6K2 may activate SREBPs and PPARs (Tables S5 and S6). Interestingly, S6K1 depletion had marginal or opposite effects on these transcription factors (Tables S5 and S6).

Since Ingenuity Pathway Analysis (IPA) upstream regulator analysis predicted enhanced activity of SREBP1/2 by S6K2 depletion (Figure 3A), we first asked if SREBPs could be contributing to the oxidative events and subsequent cell death. Depletion of S6K2 induced accumulation of cleaved SREBP1 (cl-SREBP1) (Figure S3A) and enhanced expression of SREBP-dependent lipogenic genes such as FASN and SCD1 (Griffiths et al., 2013; Jeon and Osborne, 2012; Williams et al., 2013) (Figure S3B), indicating that loss of S6K2 was coupled to activation of SREBP-dependent transcription. Silencing of SREBP1 or 2, modestly diminished cell death in S6K2-depleted cells, indicating that SREBPs were partially facilitating cell death (Figures 3B and S3C). Additionally, inhibition of SREBP-dependent lipogenic enzymes FASN and SCD1, diminished oxidation of Bodipy-C11 in S6K2-depleted cells, indicating that SREBP contributes to lipid peroxidation triggered by loss of S6K2 (Figure S3D). Additionally, incubation of S6K2-depleted cells in medium supplemented with delipidated serum did not diminish lipid peroxidation, nor protect these cells from undergoing cell death, suggesting that extracellular lipids have negligible contribution to S6K2 depletion induced lipid peroxidation and cell death (Figure S3E).

Since S6K1 stimulates the SREBP pathway (Duvel et al., 2010; Lee et al., 2017; Owen et al., 2012; Wang et al., 2011), we assessed the contribution of S6K1 to oxidative cell death in S6K2-depleted cells. Concurrent depletion of S6K1 and S6K2 attenuated SREBP1/2 cleavage, and blunted the induction of SREBP targets (Figures 3C and 3D) and

the lipid peroxidation marker PTGS2 (Yang et al., 2014) (Figures S3F and S3G). Concomitant depletion of S6K1 and S6K2 also attenuated lipid peroxidation and cell death (Figures 3E-G, S3G-I). Together, these data indicate that S6K1 is required for the effects triggered by S6K2 depletion. These results led us to postulate that selective inhibition of S6K2 in the context of active S6K1 would be required to induce lipid peroxidation and cell death in NRAS-mutant melanoma cells resistant to MAPKi. Consistent with this premise, inhibition of S6K1 with an isoform selective inhibitor (PF4708671) (Pearce et al., 2010), or concomitant inhibition of S6K1 and S6K2 with a pan-S6K inhibitor (LY2584702; LY4702) (Hollebecque et al., 2014; Tolcher et al., 2014) or a PI3K/mTOR inhibitor (GSK458) did not induce expression of lipogenic enzymes, lipid peroxidation or cell death (Figures S3J-O). In contrast, mimicking an "S6K1 on/S6K2 off" scenario by ectopically expressing constitutively active S6K1 (E389 or S389) and treating cells with LY4702 or GSK458, led to decreased viability (Figures 3H, 3I, S3P and S3Q). Collectively, these results indicate that selective inhibition of S6K2, in the context of active S6K1, induces lipid peroxidation and subsequent death of MAPKi-resistant NRAS-mutant melanoma cells.

Suppression of S6K2 relieves negative regulation on PPARα, facilitating lipid peroxidation

Transcriptomic analysis also indicated an enrichment of PPAR target genes (Kersten, 2014; Rakhshandehroo et al., 2010) in S6K2-depleted cells (Figures 4A, S4A, and Table S6). Upregulation of representative PPAR targets by S6K2 depletion was further confirmed in three MAPKi-resistant cell lines (Figure S4B). Since several PPAR targets, including those that are associated with lipid peroxidation (e.g. FADS2, PTGS2, ACSL4 and LPCAT3) (Magtanong et al., 2016; Rees et al., 2016; Viswanathan et al., 2017; Yang et al., 2014), were upregulated upon S6K2 depletion (Figures 2A, 4A, S4B and Table S6),

we sought to address whether PPAR contributed to induction of lethal lipid peroxidation. As PPAR transcriptionally regulates its own expression (Lefterova et al., 2008; Nielsen et al., 2008; Pineda Torra et al., 2002), we first examined the effects of S6K2 depletion on PPAR mRNA levels. S6K2 depletion led to upregulation of PPARα and, to a much lesser extent, PPARγ mRNA levels (Figures 4B, S4C and S4D), suggesting that PPARα might be a key effector. Consistent with this notion, silencing of PPARα prevented induction of lipid peroxidation-related genes such as FADS2 and PTGS2 by S6K2 knockdown (Figures 4C and S4E). Moreover, depletion of PPARα decreased ROS levels, lipid peroxidation and cell death in S6K2-depleted cells (Figures 4D, 4E, S4E and S4F). Conversely, treatment of NRAS-mutant melanoma cells with PPARα agonists (fenofibrate/FNB or gemfibrozil) induced ROS, lipid peroxidation and cell death (Figures S4G-H). Together, these data suggest that PPARα contributes to lipid peroxidation and cell death triggered by S6K2 depletion.

We next sought to determine the mechanism whereby S6K2 could be regulating PPARα. The transcriptional activity of PPARα is inhibited by the nuclear receptor corepressor NCoR1 (Sengupta et al., 2013), and S6K2 has been implicated in this regulation (Kim et al., 2012). Hence, we examined whether S6K2 could regulate this interaction in NRAS-mutant melanoma cells. Immunoprecipitation and proximity ligation assays (PLA) supported the existence of a complex between S6K2 and PPARα as well as its co-repressor NCoR1 (Figures 4F and S4I). S6K2 is known to shuttle between the cytosol and nucleus (Magnuson et al., 2012); therefore, we examined whether S6K2 depletion affected the localization of NCoR1 and PPARα. We found that depletion of S6K2 led to a modest decrease in the nuclear and chromatin-bound NCoR1 levels (Figure S4J). Conversely, S6K2 depletion led to an increase in chromatin-bound PPARα (Figure S4J). Notably, S6K2 depletion markedly diminished the interaction of NCoR1 with PPARα, as

assessed by PLA (Figure 4G). Together, these data support a model whereby S6K2 regulates the interaction between of NCoR1 and PPARα, and that S6K2 depletion disrupts this complex leading to activation of the PPARα axis, thereby facilitating lipid peroxidation and oxidative cell death in NRAS-mutant melanoma (Figure S4K).

Lastly, we assessed if S6K2 depletion disturbed the SREBPs and PPARα subnetworks selectively in MAPKi-resistant cells. Analysis of a panel of SREBP or PPAR targets by qRT-PCR indicated that S6K2 depletion preferentially induced the expression of these genes in MAPKi-resistant cells (Figure 4H), further supporting that SREBP and PPAR mediate imbalanced lipid metabolism and subsequent oxidative cell death triggered by S6K2 blockade in MAPKi-resistant cells.

MAPKi-resistant NRAS-mutant melanoma is sensitive to the combination of PPARα agonists and PUFA

Based on our data indicating that PPARα facilitates ROS, lipid peroxidation and cell death, we asked if PPARα agonists could induce anti-melanoma effects. We noted that PPARα (but not PPARγ) protein levels were higher in MAPKi-resistant than in MAPKi-sensitive NRAS-mutant melanoma cells (Figures 5A, S5A and S5B). These MAPKi-resistant/PPARα-high cells were more sensitive to PPARα agonists FNB and gemfibrozil than MAPKi-sensitive/PPARα-low cells (Figures 5B, S5C and S5D). Induction of lipid peroxidation and sensitivity to FNB, correlated with PPARα levels (Figures S5E-F). We also noted that while treatment with FNB increased FASN and SCD1 mRNA levels, FNB inhibited the expression of SREBP1 (Figure S5G). Therefore, we evaluated if potentiating SREBP activity or enhancing fatty acid synthesis/desaturation would better phenocopy S6K2 depletion and could further sensitize tumor cells to FNB treatment. Indeed, the SREBP activator U18666A (Schmitt et al., 2017) cooperated with FNB in triggering

oxidative cell death (Figure S5H). Likewise, addition of PUFAs (docosahexaenoic acid/DHA or arachidonic acid) potentiated the effect of FNB in inducing lipid peroxidation and cell death (Figures 5C, S5I and S5J). Of note, ROS and lipid ROS scavengers (NAC and Trolox, respectively) attenuated cell death triggered by FNB or FNB/DHA combination (Figures 5D and S5K), supporting the notion that FNB +/- DHA induce lethal lipid peroxidation. Additionally, cell death was partially rescued by inhibitors of apoptosis or ferroptosis, suggesting that FNB/DHA combination triggered both types of cell death similar to S6K2 depletion (Figure 5E). The high FNB (100 μM) combination overwhelmed the ability of apoptosis inhibitors to suppress cell death, likely by tipping the balance of cell death towards ferroptosis. Also, blocking the antioxidant defense by treating cells with erastin potentiated the effects of FNB, leading to lethal lipid peroxidation (Figure S5L). Notably, the FNB/DHA combination selectively induced lethal lipid peroxidation in MAPKi-resistant cells (Figures 5F and S5M). Taken together, these results indicate that MAPKi-resistant melanoma cells are sensitive to pharmacological activation of PPARα in combination with enhanced fatty acid desaturation or lipid peroxidation.

We then evaluated the efficacy of this approach *in vivo*. FNB significantly restrained the growth of early xenograft tumors (starting the treatment 1 week after tumor inoculation when tumors were ~40 mm^3). Enhancing fatty acid desaturation or lipid peroxidation with DHA or erastin potentiated the antitumor activity of FNB (Figure 6A). Since erastin is a tool compound, we decided to focus on the combination of FNB/DHA for further evaluation in established tumors, including syngeneic models and patient derived-xenografts/PDXs. Combining FNB with DHA induced lipid peroxidation and oxidative damage in MAPKi-resistant cell line xenografts and PDXs (Figures 6B-C and S6B-C). Importantly, FNB+DHA suppressed the growth of established NRAS-mutant MAPKi-resistant xenografts, PDXs and syngeneic tumors (Figures 6D-F) (Burd et al., 2014; Echevarria-Vargas et al., 2018)

with no overt toxicity (Figure S6D). As FNB has been shown to suppress tumor growth in mice in a non-cell autonomous manner through inhibition of angiogenesis and inflammation in host tissues (Panigrahy et al., 2008), we examined if these effects could also be contributing to the tumor suppressive activity of FNB/DHA. Treatment with FNB/DHA did not inhibit vessel density and leukocyte counts in established tumors when compared to vehicle control, suggesting that the reported angiogenesis and inflammation suppressive effects of FNB likely had negligible contribution to its antitumor activity in our models (Figures S6G-H). These results provide proof-of-principle that combining a PPARα agonist such as FNB with PUFAs facilitates lipid peroxidation, elicits anti-tumor activity, and restrains MAPKi-resistant NRAS-mutant melanoma.

Our study establishes that depletion of S6K2 perturbs redox and lipid homeostasis, thereby triggering lipid peroxidation and oxidative cell death (Figure 6G). By selectively blocking S6K2 or harnessing the S6K2 subnetwork, we have identified a strategy that could be potentially exploited as an anti-tumor approach in NRAS-mutant melanoma resistant to MAPKi.

DISCUSSION

Despite significant advances in treating melanoma, effective therapies for NRAS-mutant tumors are sorely needed. One approach to inhibiting NRAS that has been investigated is targeting its proximal downstream effectors, mainly the MAPK and PI3K pathways. While inhibiting either pathway alone is barely effective in NRAS-mutant tumors, inhibiting both pathways leads to unacceptable toxicities in patients. We hypothesized that

identifying and inhibiting convergent subnetworks, within the MAPK and PI3K super-networks, could spare the toxicities while triggering death of cancer cells.

We therefore performed a deep analysis of the signaling networks in MAPKi-resistant NRAS-mutant melanoma. By comparing the effects of MAPK inhibition in MAPKi-sensitive *vs.* MAPKi-resistant NRAS-mutant melanoma, we mapped a critical subnetwork downstream from the convergence of PI3K and MAPK. We found that a S6 kinase(S6K)-SREBP1-PPARα subnetwork is vital for cancer lipid metabolism. We uncovered that S6K is regulated primarily by the MAPK pathway in MAPKi-sensitive cells; in contrast, S6K is regulated by PI3K in MAPKi-resistant NRAS-mutant melanoma. Further, we show that uncoupling S6K1 and S6K2, by selective S6K2 depletion, triggers a lipid metabolic imbalance, leading to lipid peroxidation and cell death exclusively in MAPKi-resistant NRAS-mutant melanomas. These findings underscore that MAPKi-resistant and -sensitive cells have different signaling dependencies both upstream and downstream of mTORC1 and illustrate specialized functions of S6K isoforms, highlighting the biological importance of isoform differentiation. Moreover, the identified subnetwork might provide a strategy to pharmacologically induce lethal lipid peroxidation *in vivo*, which has been limited by the lack of compounds with sufficient bioavailability (Hangauer et al., 2017; Tsoi et al., 2018; Viswanathan et al., 2017). Of note, S6K2 KO mice are viable and develop normally (Pende et al., 2004), indicating that S6K2 is not an essential gene. Collectively, these data suggest that selective targeting of S6K2 or its effectors represents a viable opportunity for therapeutic intervention in S6K2-dependent tumors such as MAPKi-resistant NRAS-mutant melanoma. We propose a strategy to gain functional precision by targeting a S6K2 convergent subnetwork representing a vulnerability selectively in tumor cells but not in non-transformed cells.

Our study establishes that selectively depleting S6K2, without perturbing S6K1, is required to induce oxidative cell death in MAPKi-resistant NRAS-mutant melanomas. This suggests that selective inhibition of S6K2 could curb melanoma through a mechanism unachievable with PI3K or mTOR inhibitors, which inhibit both S6K1 and S6K2. However, selective S6K2 inhibitors are not yet available, in part due to the high sequence similarity of S6K2 with S6K1 and the lack of S6K2 crystal structure (Karlsson et al., 2015; Pardo and Seckl, 2013). We foresee that our findings will spur the development of such compounds, which could be valuable to target MAPKi-resistant tumors. Meanwhile, we have identified actionable targets whose modulation could be a surrogate for S6K2 inhibition and provide proof-of-concept for this strategy. We also show that MAPKi-resistant and MAPKi-sensitive NRAS-mutant melanomas exhibit different levels of phospho-ERK and PPARα, which correlate with sensitivity to MAPKi and PPARα agonists. This provides a context in which our proposed approach would be most effective.

Previous studies from our group and others have linked enhanced or persistent mTORC1/S6K signaling with acquired resistance to MAPKi in BRAF-mutant melanoma (Atefi et al., 2011; Corcoran et al., 2013; Villanueva et al., 2013) and to MEKi/Cdk4i in NRAS-mutant melanoma (Romano et al., 2018; Teh et al., 2018). Inhibition of the mTORC1/S6K axis restrains MAPK-dependent melanomas and tumors with acquired resistance to MAPKi and/or CDK4i. Likewise, sustained SREBP1 activity has been associated with resistance to BRAF inhibition in BRAF-mutant melanomas, and SREBP inhibition sensitized these tumors to MAPK blockade (Talebi et al., 2018). In contrast to strategies relying on mTOR1/S6K1/SREBP1 inhibition, we found that disrupting the S6K1/SREBP1/S6K2/PPARα subnetwork by selective S6K2 blockade leads to cell death by exploiting active lipid metabolism (Green, 2019) and accumulation of PUFAs. It would

be of interest to assess whether targeting S6K2 could induce lethality and efficiently kill other types of resistant tumors with active mTORC1/S6K1/SREBP1 signaling.

Talebi et al. reported that SREBP1-dependent lipogenesis promotes resistance to targeted therapy by limiting lipid peroxidation in BRAF-mutant melanoma (Talebi et al., 2018). Additionally, Yi et al. found that SREBP-mediated lipogenesis suppresses ferroptosis in breast and prostate cancer with hyperactive PI3K/Akt/mTOR signaling (Yi et al., 2020). Our work, in contrast, suggests that SREBP1 and its targets, FASN and SCD1, facilitate lethal lipid peroxidation in NRAS-mutant melanoma. Similarly, Song et al., found that fatty acid synthesis promotes lipid peroxidation-dependent ferroptosis in pancreatic ductal carcinoma cells (Song et al., 2021). Likely, SREBP transcriptionally regulates various lipid-related enzymes, thereby impacting lipid peroxidation in divergent manners. For example, SREBP targets can catalyze the synthesis of fatty acids (FAs) and desaturate the *de novo* synthesized or extrinsic FAs to different saturation degrees (Griffiths et al., 2013; Hagen et al., 2010). Whereas saturated or mono-unsaturated FAs limit lipid peroxidation, poly-unsaturated FAs promote lipid peroxidation. SREBP1 also regulates enzymes that channel FAs into different lipid classes (e.g. phospholipids or triglycerides) (Hagen et al., 2010), and enzymes that modulate lipid composition in membranes (Shi et al., 2013; Takeuchi and Reue, 2009), rendering lipids differentially susceptible to oxidative damage. This is further complicated, as SREBP1-regulated fatty acids can serve as ligands for PPARα (another regulator of lipid peroxidation) and its heterodimeric partner RXR (Dawson and Xia, 2012; Koundouros and Poulogiannis, 2020; Willson et al., 2000; Xu et al., 1999); thus, SREBP activation can contribute to lipid peroxidation through enhancing PPARα function. Which SREBP-mediated functions are more prominent are likely dependent on the genetic, metabolic and cellular context. Hence, it is possible that SREBP

activation and/or inhibition could trigger different phenotypes in different settings; this would need to be carefully considered when targeting SREBP-mediated processes.

In sum, our studies establish S6K2 and its effectors as a vulnerability in NRAS-mutant melanoma that are resistant to MAPKi, a tumor whose treatment remains a challenging unmet clinical need. We also identify clinically actionable surrogate targets that phenocopy the effects of S6K2 inhibition. Our results further underscore the significance of oncogenic NRAS-induced metabolic dependency and the role of S6K2 in supporting this addiction. We propose that harnessing this S6K2-dependent addiction could be exploited as a potential strategy to combat MAPKi-resistant NRAS-mutant melanoma, a highly aggressive tumor type with limited treatment options.

ACKNOWLEDGMENTS

We would like to thank Sonali Majumdar and Shashi Bala (Genomics Facility), Hsin-Yao Tang and Nicole Gorman (Proteomics and Metabolomics Facility), Joel Cassel and Isabela Batista Oliva (Molecular Screening and Protein Expression Facility), Fangping Chen and Marjorie Donnelly (Histotechnology Facility), James Hayden and Frederick Keeney (Imaging Facility), Jeffrey S. Faust (Flow Cytometry Facility), and Denise DiFrancesco (Animal Facility) at the Wistar Institute and Minu Samanta for technical support. Support for the above shared resources was provided by Cancer Center Support Grant (CCSG) P30CA010815 to the Wistar Institute. The RPPA analysis was performed by the MDACC RPPA core facility with support for shared resources provided by Cancer Center Support Grant (CCSG) CA016672 to MDACC. Support for RPPA was provided by the Dr. Miriam and Sheldon G. Adelson Medical Research Foundation.

This work was partially supported by NIH grants R01CA215733 (JV), R01CA226888 (JV), P01CA114046 (JV, MM, ZS), P50CA174523 (JV, DWS), P01CA140043 (DWS), P30CA010815, DoD W81XWH2010356 (JV), The Melanoma Research Alliance (JV), The V Foundation for Cancer Research (JV), Martha W. Rogers Trust (JV) and the PA Department of Health (JV). DZB was supported by NIH pre-doctoral training grant T32 GM008275, ARG and BL were supported by NCI NRSA T32 CA009171 Cancer Biology Training Grant to the Wistar Institute. We dedicate this work to the memory of our friends and colleagues Raj Somasundaram and Michael J. Weber.

AUTHOR CONTRIBUTIONS

H-YC, JV, MEM and DWS conceived and designed the study. H-YC, MEM, MJW, and JV wrote the manuscript. H-YC, ARG, DZ-B, PIR-U, ANG, SB, BL and MJA performed experiments, collected and analyzed data. XY and QL performed bio-statistical analysis. AVK performed bioinformatics analysis. MJW provided essential reagents. YL and GM performed RPPA. All authors contributed, reviewed and approved the manuscript.

DECLARATION OF INTERESTS

Gordon B. Mills serves as a consultant for AstraZeneca, Chrysallis Biotechnology, Immunomet, Ionis, Nuevolution, PDX Pharma, SignalChem Lifesciences, Symptomen, Tarveda; owns stock in Catena Pharma, ImmunoMet, SignalChem, Spindle Top Ventures, Tarveda; and has received research funding from AstraZeneca, Nanostring, Pfizer, Takeda/Millennium, and Tesaro. All the other authors declare no COI.

FIGURE LEGENDS

Figure 1. S6K2 is a vulnerability in NRAS-mutant melanoma resistant to MAPK inhibitors

(A) NRAS-mutant melanoma cells were treated with the MEKi trametinib (M, 10 nM) or the ERKi SCH772984 (E, 100 nM) for 48h and subjected to reverse phase protein array (RPPA) analysis. Heatmap depicts changes in protein expression or phosphorylation relative to the vehicle control (DMSO). Positive values indicate (red) upregulation; negative values (blue) indicate downregulation. Mixed-effects model was used to examine the difference between resistant versus sensitive cell lines.

(B) Cells were transduced with doxycycline-inducible wild-type S6K2 (WT) or constitutively active $S6K2^{E388}$ constructs, incubated with doxycycline for 24h, and then treated with the ERKi SCH772984 (SCH984, 1000 nM) or the PI3K/mTORi GSK2126458 (GSK458, 100 nM) for additional 24h. Percentage of $pS6^{(S240/244)+}$ cells was determined by flow cytometry. Data shown are mean ± SD (n=2); p values were determined by Student's t-test. $p<0.01$ are shown.

(C) Diagram illustrating that S6K is mainly regulated by the PI3K/mTOR pathway in NRAS-mutant melanoma cells resistant to MAPKi, whereas it can be regulated by both the MAPK and the PI3K pathways in cells sensitive to MAPKi.

(D-G) Cells were transduced with lentiviruses encoding S6K1 or S6K2 shRNA.

(D) Cell death in MAPKi-resistant cells was analyzed by PSVue/PI staining (6-7 days post infection; dpi). Data shown are mean ± SD (n=2 or 3 independent experiments).

(E) Levels of S6K1/2 and cleaved-caspase 3 were analyzed by immunoblotting. Numbers below each blot indicate protein quantification relative to actin.

(F) Cell death in MAPKi-sensitive cells. Data are mean ± SD (n=2 independent experiments).

(G) Percent cell death induced by S6K1 or S6K2 depletion in three MAPKi-R (D) and three MAPKi-S (F) cell lines was compared by unpaired, two-tailed Student's t-test. Data from each condition (vector, S6K1 sh1/4 and sh5, or S6K2 sh1 and sh4) were pooled and shown as mean ± SEM; n.s.: not significant.

*$p < 0.05$, **$p < 0.01$ and ***$p < 0.001$.

(H) Inverse correlation of S6K1 vs. S6K2 gene expression for 470 patients from the Skin Cutaneous Melanoma TCGA database.

(I) Kaplan-Meier survival curve analysis was performed using R2: Genomics Analysis and Visualization for a TCGA melanoma dataset (470 patient samples total). Samples were classified into high- or low- S6K1 or S6K2 expressing groups according to the average tissue mRNA expression levels. Survival curves are depicted for the patient cohort that received targeted therapies (Vemurafenib, Dabrafenib, Trametinib) as one of their treatments (N=355).

See also Figure S1.

Figure 2. Depletion of S6K2 triggers lipid peroxidation facilitating cell death

NRAS-mutant melanoma cells were transduced with lentiviruses encoding S6K1 or S6K2 shRNA, or non-targeting vector control (Vec).

(A-B) Transduced M93-047 cells were subject to (A) proteomic or (B) lipidomic analysis (4 dpi).

(A) Heatmap depicting relative abundance of selected proteins associated with lipid metabolism or lipid peroxidation (log2 ratio of shRNA *vs.* vector). p values were determined by Student's t-test.

(B) Box and whiskers plot depicting diacyl glycerophospholipids differentially affected by S6K2sh *vs.* S6K1sh (two-tailed Student's t-test, $p<0.05$ S6K2sh *vs.* S6K1sh). Each dot indicates individual lipid species. Details of individual lipid are presented in Figure S2D.

(C) Transduced cells (6 dpi) were stained with the ROS sensing dye H2DCFDA and analyzed by flow cytometry.

(D) Transduced cells (6 dpi) were stained with the lipid ROS/lipid peroxidation sensor Bodipy-C11 and analyzed by flow cytometry. Dashed line indicates the gate for Bodipy-C11+ cells.

(E) Transduced M93-047 cells (2 dpi) were treated with the ROS scavenger NAC (1 mM) for additional 3 days and cell death was assessed.

(F, H) M93-047 cells were transduced with lentiviruses encoding S6K2 shRNA or non-targeting vector control.

(F) Transduced cells (1 dpi) were treated with the lipophilic ROS scavenger trolox (100 μM) for 3 days, and analyzed for cell death.

(G) Three MAPKi-R and four MAPKi-S cell lines were transduced with lentiviruses encoding S6K2 shRNA, S6K1 shRNA or non-targeting vector control for 6-7 days and assessed for levels of ROS (H2DCFDA) or lipid ROS (Bodipy-C11). See also Figure S2L. Two-group t-test was used to compare the average in fold change between MAPKi-R *vs.* MAPKi-S. Bonferroni's adjusted p-values are reported.

(H) Transduced cells (1 dpi) were treated with inhibitors of necroptosis (necrostatin-1/Nec-1, 20 μM), ferroptosis (ferrostatin-1/Fer-1, 2 μM), apoptosis (zVAD, 20 μM), or combination of Fer-1 and zVAD for additional 3 days, and analyzed by PSVue/PI staining.

(E, F, H). Data represent mean ± SD (n=2) of one representative experiment.

Statistical significance was assessed by Student's t-test. * $p<0.05$, ** $p<0.01$, *** $p<0.001$.

See also Figure S2.

Figure 3. S6K1 and SREBP1 contributes to oxidative cell death

Experiments were performed in M93-047 MAPKi-resistant NRAS-mutant melanoma cells.

(A) Cells were transduced with S6K1 or S6K2 shRNA (3 dpi) and analyzed by RNA-sequencing. Genes significantly altered by S6K2 depletion were analyzed by IPA (Ingenuity Pathway Analysis); activation of SREBP (*SREBF*) was predicted based on changes of its known targets. Heatmap showing z-scores of the prediction. ns: no significant enrichment of targets.

(B) Cells were transfected with SREBP1 or SREBP2 siRNA followed one day later by transduction with an empty vector control (Vec) or S6K2 shRNA. Cell death was assessed 6dpi. Data shown are mean ± SD (n=2).

(C-G) Cells were transduced with lentiviruses encoding S6K2 shRNA + Vector or S6K1 shRNA.

(C) Levels of cleaved SREBP1 or SREBP2 were assessed by immnoblotting.

(D) Expression of SREBP1 and SCD1 was assessed by qRT-PCR (3 dpi). Data are mean ± SD (n=3).

(E) Lipid peroxidation was assessed in transduced cells (6 dpi). Horizontal bars indicate gates for Bodipy-C11+ cells.

(F) Cell death was determined 4 dpi. Data are shown as mean ± SD (n=2).

(G) PTGS2 and cleaved caspase 3 levels were determined by immunoblotting.

(H-I) Cells were transduced with doxycycline inducible $S6K1^{E389}$; cells were treated with doxycycline (Dox) and LY4702 (10 μM) for two days.

(H) Expression of S6K1 was determined by immunoblotting (left panel) and pS6 $^{(S240/244)}$ was assessed by flow cytometry (right panel). Data are mean ± SD (n=2).

(I) Cell viability was determined by crystal violet staining 7 days post treatment. Data are shown as mean ± SD (n=3-4).

(B, D, F, H and I) One representative experiment.

Statistical significance was assessed by Student's t-test; * $p<0.05$, ** $p<0.01$, *** $p<0.001$, n.s., not significant.

See also Figure S3.

Figure 4. Suppression of S6K2 relieves negative regulation on PPARα facilitating lipid peroxidation

(A-G) M93-047 cells were transduced with S6K1 or S6K2 shRNA.

(A) Transduced cells (3 dpi) were analyzed by RNA sequencing. Heatmap depicts mRNA expression levels of selected PPAR target relative to mean across samples.

(B) PPAR mRNA expression was determined by qRT-PCR (4 dpi). Data are shown as mean ± SD (n=3). See also Figure S4C.

(C-D) Cells were transduced with PPARα shRNA 36 h prior to S6K2 shRNA.

(C) FADS2 and PTGS2 levels were determined by qPCR (4 dpi S6K2 shRNA). Data are shown as mean ± SD (n=3). See also Figure S4E.

(D) Transduced cells (5-6 dpi S6K2 shRNA) were analyzed for H2DCFDA (upper), Bodipy-C11 (bottom). See also Figure S4E.

(E) S6K2 shRNA and/or PPARα shRNA transduced cells (6-7 dpi) were analyzed for cell death. Data are shown as mean ± SD (n=2). See also Figure S4F.

(F) Interaction of S6K2 with PPARα or NCoR1 was determined by proximity ligation assay (PLA). Left: Representative images. Scale bar = 30 μm. Right: Bar graphs show quantification of images. Data indicate mean ± SD (n denotes numbers of cells). S6K2 Ab, PPARα Ab or NCoR1 Ab indicates single antibody controls.

(G) PLA was performed in transduced cells (4 dpi). Top: Representative images. Scale bar = 30 μm. Bar graphs show quantification of images (Bottom left). Data represent mean ± SD (n denotes fields quantified). S6K2 mRNA levels (4 dpi) were assessed by qRT-PCR (Bottom right). Data shown are mean ± SD (n=3).

(H) MAPKi-R or MAPKi-S NRAS-mutant melanoma cell were transduced with S6K2 shRNA. Expression of SREBP or PPAR targets was determined by qRT-PCR (4 dpi). Data are shown as mean ± SD (n=3).

(B, C, E, H) One representative experiment.

Statistical significance was assessed by Student's t-test. * $p<0.05$, ** $p<0.01$, *** $p<0.001$. See also Figure S4.

Figure 5. PUFAs potentiate the oxidative cell death inducing effect of PPARα agonists

(A) Relative expression of PPARα in MAPKi-R (red) and MAPKi-S (blue) cells determined by immunoblotting (see Figure S5A), was compared by Student's T-test. Data represent average PPARα levels from two independent experiments.

(B) AUC for MAPKi-R and MAPKi-S cells (shown in Figure S5C) were compared by Student's T-test.

(C) Cells were treated with fenofibrate, DHA, as single agents or in combination for 72 h. Lipid peroxidation and cell death were assessed by Bodipy-C11 and PSVue/PI staining, respectively. % Cell death is shown in bar graphs as mean ± SD (n=2).

(D) Cells were treated with fenofibrate, DHA, as single agents or in combination ± the lipophilic ROS scavenger trolox (100 μM) for 72 h. ROS, lipid peroxidation and cell death were assessed by H2DCFDA, Bodipy-C11 and PSVue/PI staining, respectively. % Cell death is shown in bar graphs as mean ± SD (n=2).

(E) Cells were treated with fenofibrate, DHA, as single agents or in combination ± the ferroptosis (ferrostatin-1/Fer-1, 2 μM) or apoptosis (zVAD, 20 μM) inhibitors for 72h, and analyzed by PSVue/PI staining. % Cell death is shown in bar graphs as mean ± SD (n=2).

(F) MAPKi-R and MAPKi-S cells were treated with fenofibrate, DHA, as single agents or in combination for 72 h. Cell death was assessed by PSVue/PI staining. Each dot represents an individual cell line.

Statistical significance was assessed by Student's t-test. * $p<0.05$, ** $p<0.01$, *** $p<0.001$. See also Figure S5.

Figure 6. MAPKi-resistant NRAS-mutant melanoma is sensitive to the combination of PPARα agonists and PUFA

(A) Mice bearing M93-47-derived subcutaneous tumors (~40 mm3) were treated with fenofibrate (200 mg/kg), DHA (300 mg/kg) or erastin (30 mg/kg, bid.qod) as single agents or in combination. Data are shown as mean ± SEM. Veh, FNB, erastin (n=10); FNB+DHA, FNB+Erastin (n=9). FDR adjusted p-values were estimated from a linear mixed-effect model with all follow-up subjects and time points.

(B-C) Mice bearing WM4023 (PDX), WM1366 or WM3623 xenografts were treated with fenofibrate (200 mg/kg) or DHA (300 mg/kg) as single agents or in combination for 7 days. Tumors were analyzed by immunohistochemistry for 4-HNE. (B) Representative images. Scale bar = 25 μm. (C) Quantification of 4-HNE staining using QuPath software. Bar graphs show H-score from representative fields (Mean ± SEM; WM4023 n=2, WM1366 and WM3623 n=3 to 4 each treatment group).

(D) Mice bearing M93-047-derived xenografts were treated with vehicle (n=9), fenofibrate (200 mg/kg, n=10), DHA (300 mg/kg, n=9) or fenofibrate + DHA combination (n=8) when tumors reached ~150 mm^3 (12 days post inoculation).

(E) C57Bl/6 mice bearing *LSL-Nras*$^{Q61R/Q61R}$ *(TpN*$^{61R/61R}$*)* syngeneic tumors were treated with vehicle (n=8), fenofibrate (200 mg/kg, n=9), DHA (300 mg/kg, n=8) or fenofibrate+DHA combination (n=8) when tumors reached ~85 mm^3 (19 days post inoculation).

(D and E) P-values and FDR adjusted p-values were estimated from a linear mixed-effect model with all follow-up subjects and time points.

(F) Mice were given control chow or DHA (0.15% w/w) plus FNB (0.15% w/w) laced chow when when tumors reached ~140 mm^3 (WM4023, control n=5, DHA+FNB n=4) or ~110 mm^3 (WM4299-1, control n=5, DHA+FNB n=5). Mice were followed until tumors reached a pre-defined volume (1200 mm^3). P values were calculated using log-rank (Mantel-Cox) test.

(G) Proposed model illustrating that uncoupling S6K1 and S6K2 triggers oxidative cell death in NRAS-mutant melanoma resistant to MAPKi.

See also Figure S6.

Figure S1. Related to Figure 1. MAPK and PI3K/mTOR differentially regulate S6K in NRAS-mutant melanoma cells sensitive *vs.* resistant to MAPK inhibitors

(A) NRAS-mutant (Q61K/R/L) melanoma cells were treated with the MEKi trametinib (Tram; 0.1-1000 nM) or the ERKi SCH772984 (SCH984; 1-10 μM) for 72h and cell viability was assessed by MTT assays. Area under the dose-response curve (AUC) was calculated as a measure of drug sensitivity.

(B- C) Cells were treated with trametinib (100 nM) or SCH772984 (1000 nM) for 72h.

(B) BrdU incorporation relative to DMSO. Data represent mean ± SD (n=3). The difference of BrdU incorporation between DMSO- and drug-treated cells was calculated in each cell line. Suppression of BrdU incorporation in MAPKi-R and MAPKi-S cells was compared by unpaired, two-tailed Student's t-test.

(C) Cell death was assessed by PSVue/PI staining an analyzed by flow cytometry. Data are mean ± SD (n=2). Cell death induction was calculated in each cell line, and compared in MAPKi-R *vs.* MAPKi-S cells using unpaired, two-tailed Student's t-test.

(D) NRAS-mutant melanoma cells were treated with SCH772984 (1000 nM) for 24h and analyzed by immunoblotting.

(E) Cells were treated with trametinib (100 nM) or SCH772984 (1000 nM) for the indicated times and analyzed by immunoblotting.

(F) Cells were treated with increasing doses of the MEKi MEK-162 or the ERKi BVD-523 for 72h and relative cell viability was determined by CellTiter-Glo. Data are mean ±SEM (n=2).

(G) Basal levels of pERK were determined by immunoblotting. Gap indicates samples ran on different gels. Blots were quantified and pERK levels were normalized to actin (loading control); M93-047 lysate was run on both blots and pERK levels were normalized accordingly. Average pERK basal levels in MAPKi-R and MAPKi-S cells from two

independent experiments were compared by unpaired t-test (bottom panel).

(H) Scatterplot depicting inverse correlation between sensitivity of NRAS-mutant melanoma cells to the MEKi trametinib or the ERKi SCH772984 (defined by AUC) and basal pERK levels.

(I) Cells were treated with the PI3K/mTORi GSK458 (0.1 μM) for 24h; $pS6^{(S240/244)}$ levels were assessed by immunoblotting.

(J) Cells were treated with the PI3Ki LY294002 (10 μM), the PI3K/mTORi GSK458 (0.1 μM), or the mTORi INK128 (0.1 μM); phosphorylation of S6 was determined by immunoblotting. All samples were run on the same gel (gaps indicate where lanes were removed for simplicity).

(K) Cells transduced with doxycycline-inducible $S6K1^{E389}$ were incubated with doxycycline for 24h and then treated with SCH984 (1000 nM) or GSK458 (100 nM) for additional 24h. Percentage of $pS6^{(S240/244)+}$ cells was assessed by FACS. Data represent mean ± SD (n=2); ***$p<0.0001$ determined by Student's t-test are shown.

(L-M) Cells were transduced with lentiviruses encoding S6K1 or S6K2 shRNA.

(L) Transduced cells (6 dpi) were labeled with BrdU (4h), stained with PI and analyzed by flow cytometry. Percentage of BrdU+ cells is depicted in the upper right corner.

(M) S6K1 or S6K2 knockdown efficiency was assessed by qRT-PCR**.** Data represent mean ± SD (n=3).

(N) MAPKi-R cells were transduced with lentiviruses encoding two additional S6K2 shRNAs for 6-7 days. Knockdown efficiency of S6K2 was assessed by immunoblotting (upper panel). Cell death was determined by PSVue/PI staining (FACS; bottom panel). Data represent mean ± SD (n=2).

(O) MAPKi-S cells were transduced with lentiviruses encoding S6K1 or S6K2 shRNA for 6-7 days. Knockdown efficiency of S6K1 or S6K2 was assessed by qRT-PCR. Data

represent mean ± SD (n=3). (Related to Figure 1F).

(P) Human fibroblasts were transduced with lentiviruses encoding shRNA against S6K1 or S6K2 for 6 days. Knockdown efficiency for S6K1 or S6K2 was assessed by immunoblotting (upper panel). Cell viability was determined by MTT assays (bottom panel). Data are shown as mean ± SD (n=7).

(B, C, G, M-P) Statistical significance was calculated by Student's t-test; ** $p<0.01$, *** $p<0.001$, n.s. not significant.

Figure S2. Related to Figure 2. Depletion of S6K2 perturbs lipid metabolism and leads to widespread oxidative damage and cell death

(A) NRAS-mutant melanoma cells transduced with lentiviruses encoding S6K1 or S6K2 shRNA or vector control (Vec) were subject to LC-MS/MS proteomic analysis (4 dpi). Schematic depicts analysis of proteomics data identifying lipid metabolism and redox balance as processes disrupted by S6K2 depletion. Proteins selectively affected by S6K2 shRNA were ranked by fold change (Student's t-test $p<0.05$ shS6K2 *vs.* Vec; proteins significantly affected by S6K1sh, $p<0.05$ shS6K1 *vs.* Vec, were omitted). Pathways/biological processes for the top proteins were overlaid with IPA canonical pathway analysis results and color coded.

(B) Transduced cells (4-6 dpi) were analyzed by reverse phase protein array. Heatmap depicts fold change ($\log_2$) of shRNA/vector. P-values were calculated by comparing effect of S6K1sh *vs.* S6K2sh for different cell lines.

(C) Lipidomic analysis was performed in transduced M93-047 cells (4 dpi). Triacylglycerol content (upper panel) and percentage of TG subclasses in each treatment (bottom panel). Data represent mean ± SD (n=3). Lipid content was normalized to total lipid area for each sample.

(D) Heatmap depicting diacyl glycerophospholipids (log_2 ratio shRNA *vs.* vector) differentially affected by S6K2sh *vs.* S6K1sh (two-tailed Student's t-test, $p<0.05$ S6K2sh *vs.* S6K1sh). Lipid species are categorized by fatty acid composition.

(E) M93-047 cells transduced with two different S6K2 shRNAs were stained with Bodipy-C11 and analyzed by flow cytometry. Dashed line indicates the gate for Bodipy-C11+ cells.

(F-K) M93-047 cells were transduced with lentiviruses encoding S6K1 or S6K2 shRNA.

(F-G) Cells (6 dpi) were stained for 4-HNE adducts and analyzed by flow cytometry (F) or immunofluorescence (G). Scale bar = 100 μm.

(H-I) Transduced cells (6 dpi) were stained with the DNA/RNA damage marker, 8-OHdG, and analyzed by flow cytometry (H) or immunofluorescence (I). Scale bar = 100 μm.

(J-K) DNA double strand breaks were assessed in M93-047 cells by p-γH2AX (6 dpi, flow cytometry) (J) or 53BP1 staining (8 dpi, immunofluorescence) (K).

In J, data represent mean ± SEM (n=2). In K, quantification of cells > 7 foci in six fields is depicted (mean ± SEM).

(L) NRAS-mutant melanoma cells transduced with lentiviruses encoding S6K2 shRNA, S6K1 shRNA or non-targeting vector control for 6-7 days, stained with H2DCFDA or Bodipy-C11 and analyzed by flow cytometry.

(M) PTGS2 levels were determined in S6K1- or S6K2-depleted M93-047 cells. Top panel: reverse phase protein array (4dpi). Bottom panel: qRT-PCR. S6K1sh, 4d doxycycline induction; S6K2sh, 4dpi). Data represent mean ± SD (n=3).

(N) S6K2-depleted M93-047 cells (1 dpi) were treated with ferrostatin-1 (Fer-1, 2 μM) or liproxstatin-1 (Lip1, 1 μM) for 8 days, and analyzed by PSVue/PI staining. Data represent mean ± SD (n=2).

(O) Transduced cells (2 dpi) were treated with the iron chelator DFO (5 μM) for additional 4 days, and analyzed by Bodipy-C11 (left) or PSVue/PI staining (right).

(B, C, J, K, M, N and O) Statistical significance was assessed by Student's t-test. * $p<0.05$, ** $p<0.01$, *** $p<0.001$.

Figure S3. Related to Figure 3. Concomitant suppression of S6K1 and S6K2 diminishes the effects of S6K2 depletion

(A-H) NRAS-mutant melanoma cells (M93-047, unless otherwise indicated) were transduced with S6K1 and/or S6K2 shRNA.

(A) Cleaved SREBP1 and SREBP2 (cl-SREBP1/2) was assessed by immunoblotting in S6K2-depleted cells (3 dpi). cl-SREBP levels were quantified and normalized to actin; numbers below each lane indicate normalized cl-SREBP levels relative to vector control.

(B) Expression of a panel of SREBP target genes was assessed in S6K2 shRNA-transduced cells (4 dpi) by qRT-PCR. Data represent mean ± SD (n=3).

(C) S6K2 and SREBP1/2 mRNA levels for data shown in figure 3B were determined by qRT-PCR (3-day post siRNA transfection and 2 dpi S6K2sh).

(D) S6K2-depleted cells (1-2 dpi) were treated with the FASN inhibitor GSK2194069 (left panel; 0.1 μM, 3 days) or the SCD1 inhibitor A939572 (right panel; 5 μM, 3 days). Cells were stained with Bodipy-C11 and analyzed by flow cytometry. Horizontal bars indicate gates for Bodipy-C11+ cells.

(E) S6K2-depleted cells were incubated in regular serum (RS) or delipidated serum (LDS) (6 dpi), stained with Bodipy-C11 or PSVue/PI and analyzed by flow cytometry.

(F) Expression of PTGS2 (4 dpi) was assessed by qRT-PCR. Results from one representative experiment are shown as mean ± SD (n=3).

(G) S6K1 and S6K2 mRNA levels for data shown in figures 3D-F and S3F were determined by qRT-PCR (4 dpi).

(H) Cells were transduced with lentiviruses encoding S6K2 shRNA + Vector or S6K1 shRNA (sh1/4, a different set from Figure 3F) and assessed for cell death (6 dpi, left panel). Knockdown efficiency of S6K1 or S6K2 were determined by qRT-PCR (4 dpi, middle and right panels).

(B, C, F, G and H) Data from a representative experiment are shown as mean ± SD (n=3). *** $p<0.001$; n.s., not significant.

(I) Representative images of cells transduced with the indicated shRNAs (10 dpi). Scale bar = 300 μm.

(J-L) M93-047 cells were treated with the S6K1i PF4708671 (10 μM) or the pan-S6Ki LY2584702 (LY4702, 10 μM) for 48h.

(J) Expression of genes involved in lipogenesis was determined by qRT-PCR.

(K) Lipid peroxidation was determined by Bodipy-C11.

(L) Cell death was assessed by PSVue/PI staining. Suppression of S6K activity was determined by immunoblotting of pS6 (inset). All proteins were run on the same gel (gaps denote lanes that were removed for simplicity).

(M-O) NRAS-mutant cells were treated with the PI3K/mTOR inhibitor GSK458 (0.05 μM).

(M) Expression of lipid synthesis genes was determined by qRT-PCR after 24h of treatment.

(N) Lipid peroxidation was determined by Bodipy-C11 staining after 24h treatment.

(O) Cell death was determined by PSVue/PI staining 72h post treatment. Inhibition of S6K was assessed by immunoblotting of pS6 24h post treatment (inset).

Data from one representative experiment are shown as mean ± SD (n=3 for I and L, and n=2 for N and K).

(P-Q) M93-047 cells were transduced with empty vector control (Vec) or FLAG-tagged $S6K1^{S389}$. Transduced cells were then treated with DMSO (-), the pan S6Ki LY4702 (10

μM) (P) or the PI3K/mTORC1i GSK458 (0.1 μM) (Q) for 48h. Transduced cells were analyzed by immunoblotting with the indicated antibodies. Cell death was determined by PSVue/PI staining and flow cytometry. Results are mean ± SD (O, n=4; P, n=2). Statistical significance was assessed by Student's t-test. * $p<0.05$, ** $p<0.01$, *** $p<0.001$, n.s., not significant.

Figure S4. Related to Figure 4. PPARα facilitates cell death induced by S6K2 silencing

(A) M93-047 cells were transduced with S6K1 or S6K2 shRNA (3 dpi) and analyzed by RNA sequencing. Genes significantly altered by S6K2 depletion were analyzed by IPA. Heatmap depicts Z-scores for predicted activity of regulators in the PPAR family or PPAR-modulating compounds. Positive/red = activated; negative/blue = inhibited by S6K1 or S6K2 shRNA; ns: no significant enrichment of known targets.

(B) Cells were transduced with S6K2 shRNA (4dpi). mRNA expression of PPAR-regulated genes was determined by qRT-PCR.

(C) S6K2 mRNA expression of S6K2-depleted cells for figure 4B was determined by qRT-PCR (4 dpi).

(D) PPAR mRNA levels were analyzed by qRT-PCR in S6K1-depleted cells (4 dpi).

(E) Cells were transduced with PPARα shRNA 36 h prior to S6K2 shRNA. S6K2 (4 dpi) and PPARα (5.5 dpi) levels for figures 4C-D were determined by qPCR.

(F) Cells were transduced with S6K2 and/or PPARα shRNAs. S6K2 (3 dpi) and PPARα (5 dpi) mRNA levels for figure 4E were determined by immunoblotting and qPCR respectively.

(G-H) Cells were treated with the indicated concentrations of PPARα agonists, fenofibrate (G) or gemfibrozil (H) for 3 days and analyzed by H2DCFDA, Bodipy-C11 or PSVue/PI

staining. Data from a representative experiment are shown; bar graphs depict mean ± SD (n=2).

(I) S6K2 immunoprecipitation and immunoblotting with the indicated antibodies in M93-047.

(J) Transduced cells (4 dpi) were fractionated into cytosol (CE), nuclear (NE) and chromatin-bound (ChB) fractions and analyzed by immunoblotting. WE: whole cell extract. Protein levels relative to vector control are shown below each band.

(K) Proposed model illustrating regulation of PPARα by S6K2.

(B-E, F bottom panel) Data shown are mean ± SD (n=3).

Statistical significance was assessed by Student's t-test; * $p<0.05$, ** $p<0.01$, *** $p<0.001$.

Figure S5. Related to Figure 5. Combining PPARα agonists and PUFA mimics the effects of S6K2 inhibition in NRAS-mutant melanoma resistant to MAPKi

(A) PPARα and PPARγ levels in MAPKi-R and MAPKi-S cells were determined by immunoblotting. PPARα/γ levels were normalized to actin (loading control); numbers indicate protein levels relative to UACC1273.

(B) Relative levels of PPARγ in MAPKi-R and MAPKi-S cells shown in A were compared by Student's t-test.

(C) MAPKi-R (red) and MAPKi-S (blue) cells were treated with increasing doses of fenofibrate for 72h; cell viability was determined by CellTiter-Glo. Data represent average from two independent experiments ± SD.

(D) MAPKi-R (red) and MAPKi-S (blue) cells were treated with the PPARα agonist gemfibrozil (400 μM) for 72 h and assessed for cell death. Data represent average from two to four independent experiments ± SEM.

(E) Scatterplot depicting correlation between lipid peroxidation induced by fenofibrate and

PPARα levels (values from Figure 5A).

(F) Scatterplot depicting correlation between sensitivity of NRAS-mutant melanoma cells to the PPARα agonist fenofibrate (defined by AUC derived from Figure S5C) and PPARα levels (values from Figure 5A).

(G) mRNA expression was determined by qRT-PCR in M93-047 cells treated with the indicated doses of fenofibrate for 24h. Data from a representative experiment are shown as mean ± SD (n=3).

(H) M93-047 cells were treated with the SREBP1 activator U18666A (2.5 μM) and fenofibrate (25 or 50 μM) as single agents or in combination for 72h. Cell death was determined by PSVue/PI staining.

(I) Cells were treated with fenofibrate, DHA, as single agents or in combination for 72 h. ROS production was assessed by H2DCFDA staining.

(J) WM1366 cells were treated with fenofibrate (50 μM) and increasing doses (15-60 μM) of arachidonic acid as single agents or in combination for 72h. Lipid peroxidation (left) and cell death (right) were measured by Bodipy-C11 and PSVue/PI staining respectively.

(K) WM1366 cells were treated with fenofibrate, DHA, as single agents or in combination ± the ROS scavenger NAC (1 mM) for 72 h. ROS, lipid peroxidation and cell death were assessed by H2DCFDA, Bodipy-C11 and PSVue/PI staining, respectively. Data from a representative experiment are shown in bar graphs as mean ± SD (n=2).

(L) WM1366 cells were treated with fenofibrate ± erastin for 72h. Lipid peroxidation and cell death were determined by Bodipy-C11 (left) and PSVue/PI staining (right), respectively.

(H, J-L) Data from a representative experiment are shown as mean ± SD (n=2).

(M) Cells were treated with fenofibrate, DHA, as single agents or in. ROS and lipid peroxidation were assessed by H2DCFDA and Bodipy-C11 staining, respectively. Each dot indicates individual cell line.

Statistical significance was assessed by Student's t-test; * $p<0.05$, ** $p<0.01$, *** $p<0.001$.

Figure S6. Related to Figure 6. Mimicking the effects of S6K2 suppression restrains NRAS-mutant melanoma resistant to MAPKi

(A) Mice bearing WM4023 or WM4299-1 patient-derived xenografts (~85 or 70 mm^3) were treated with the MEK inhibitor PD0325901 (1.5 or 5 mg/kg). Data are shown as mean ± SEM, n=4 mice/treatment group. FDR adjusted p-values were estimated from a linear mixed-effect model with all follow-up subjects and time points.

(B-C) Mice bearing M93-047, WM4023 (PDX) or WM3623 xenografts were treated with fenofibrate (200 mg/kg), DHA (300 mg/kg) as single agents or in combination for 7 days. Tumors were analyzed by immunohistochemistry for 8-OHdG. (B) Representative images. Scale bar = 25 µm. (C) Quantification of 8-OHdG nuclear staining using QuPath software. Bar graphs show H-score from representative fields (Mean ± SEM; M93-047 and WM4023 n=2, WM3623 n=3 each treatment group).

(D) Weight of animals enrolled in the study depicted in Figures 6D-E at the last follow-up time points (day 24 and 30 respectively). Mice were treated with fenofibrate (200 mg/kg) or DHA (300 mg/kg) as a single agent or in combination. Data are shown as mean ± SEM.

(E-F) Mice bearing cell line-derived xenografts were treated with vehicle, fenofibrate (200 mg/kg), DHA (300 mg/kg) or fenofibrate+DHA combination. (See also Figure 6D). Tumors at day 24 (M93-047, see also Figure 6D) or day 7 (WM1366) were analyzed by CD31 or CD45 immunohistochemistry. (E) CD31 or CD45 positive tumor cells were quantified by QuPath software. Bar graphs show CD31+ area/total tumor area or % of CD45+ cells from

representative fields (Mean ± SEM; M93-047 n=2 to 3, WM1366 n=3 to 4 each treatment group). (F) Representative images from M93-047 xenografts. Scale bar = 50 μm.

(C-E) P-values were assessed by Student's t-test. * $p<0.05$, ** $p<0.01$.

STAR METHODS

CONTACT FOR REAGENT AND RESOURCE SHARING

Further information and requests for resources and reagents should be directed to the lead contact, Jessie Villanueva (jvillanueva@wistar.org).

EXPERIMENTAL MODEL AND SUBJECT DETAILS

Cells and culture conditions

Human fibroblasts (FF2511) were isolated from deidentified neonatal foreskin samples and maintained in RPMI1640 (Corning #10-040-CM) containing heat-inactivated 10% fetal bovine serum (FBS). Melanoma cell lines and 293T cells were grown in RPMI1640 supplemented with 5% and 10% FBS respectively. All cells were maintained at 37°C in 5% CO2. FBS was purchased from Tissue Culture Biologicals (#101; Lot#170708, 105094, 101258) or Clontech (#631107; Lot#A301117007). Lipid-depleted serum was prepared by treating with Cleanascite reagent (Biotech Support Group #X2555) at a volume ratio of 1:4 per the manufacturer's instructions.

Cell lines were authenticated by human microsatellite analysis at 5 different loci using Coriell Identity Mapping Kit (Coriell Institute for Medical Research) or at 16 different loci using the AmpFLSTR™ Identifiler™ PCR Amplification Kit (Thermo Fisher Scientific #4322288) at the Wistar Institute Genomics Facility, and screened for mycoplasma using MycoAlert Mycoplasma Detection Kit (Lonza #LT07-318).

Drug treatments

Erastin was diluted to the final concentration in fresh growth medium and conditioned medium (1:1) and added to the cells. Other drugs were diluted into fresh growth medium and added to the cells.

Animal Studies

All animal studies were approved by the Institutional Animal Care and Use Committee (IACUC) at the Wistar Institute and performed in accordance with institutional guidelines. Mice were housed in groups of five/cage in an Association for the Assessment and Accreditation of Laboratory Animal Care (AAALAC) certified facility. NOD/LtScidIL2Rγ-null mice (NSG) male and female mice (4 to 8-week-old, ~ 25-30 g) were procured from The Wistar Institute. C57Bl/6 mice (4-week-old, ~25 g) were obtained from Charles River.

For *in vivo* xenograft studies, 1 x 10^6 cells were resuspended in 1:1 RPMI1640/Matrigel (Matrigel Matrix, Corning #354230) and implanted subcutaneously into the flanks of male NSG mice. Patient-derived xenografts were minced, mixed with Matrigel and implanted into male NSG mice.

For the syngeneic mouse model, Nras-mutant tumors (WHN89) were derived from *Tyr-CRE-ER^{T2} p16$^{L/L}$ LSL-Nras$^{Q61R/Q61R}$ (TpN$^{61R/61R}$)* mouse model (Burd et al., 2014). *TpN$^{61R/61R}$* tumors were minced and implanted into male C57Bl/6 mice.

Tumor volume was measured using digital calipers and calculated by length x width^2/2.

Mice in all treatment groups were euthanized when the vehicle-treated group reached the humane endpoint (tumor volume 1500-2000mm^3).

In vivo drug treatments

PD0325901 treatment:

Patient-derived xenografts were minced and subcutaneously injected into 8-week-old male NSG mice. When tumors reached 100-150 mm^3, mice were randomly assigned into experimental groups. PD0325901 was prepared in 0.2% Tween 80 + 0.5% hydroxypropyl-methyl cellulose + 3% DMSO in ddH2O and administered by oral gavage (1.5 or 5 mg/kg/day).

Fenofibrate combination:

M93-047 cells were subcutaneously injected into 8-week-old male NSG mice. One week after tumor cell inoculation (tumor size ~ 40 mm^3), mice were randomly assigned into five experimental groups: vehicle, fenofibrate, erastin, fenofibrate + DHA, or fenofibrate + erastin. Fenofibrate suspension was prepared in 4% DMSO + 40% PEG300 + 2% Tween 80 in ddH2O and administered by oral gavage (200 mg/kg/day). Erastin was dissolved in vehicle (9% DMSO + 20% Tween 80 in PBS) and injected at the tumor site (30 mg/kg, twice daily, every other day). DHA was administered by oral gavage (300 mg/kg/day) in soybean oil.

To study the effect of therapy in established tumors, M93-047 cells or minced patient-derived xenografts were subcutaneously injected into 4-week-old male NSG mice. When tumors reached 100-200 mm^3, mice were randomly assigned into experimental groups.

Syngeneic *TpN*$^{61R/61R}$ tumor cells (WHN89) were subcutaneously injected into 4-week-old male C57Bl/6 mice. When tumors reached ~85 mm^3, mice were randomly assigned into experimental groups. Mice bearing patient-derived xenografts were given control chow or DHA (0.15% w/w) plus FNB (0.15% w/w) laced chow.

METHOD DETAILS

Source of compounds and chemicals

Cayman chemical: Arachidonic acid (#90010), BVD-523 (#18298), Docosahexaenoic Acid (DHA; Cayman Chemical #90310 & MedChemExpress #HY-B2167/CS-6261), Fenofibrate (#10005368), Gemfibrozil (#14835), GSK2126458 (#17377), GSK2194069 (#20022), INK128 (#11811), LY294002 (#70920), MEK-162 (#16996), Necrostatin-1 (#11658), SCH772984 (#19166), U-18666A (#10009085), zVAD (zVAD(OMe)-FMK, #14463).

Selleckchem: Erastin (#S7242), Ferrostatin-1 (#S7243), Liproxstatin-1 (#S7699), LY2584702 (LY2584702 Tosylate, #S7704), PF4708671 (#S2163), Trametinib (#S2673).

Sigma-Aldrich: BrdU (5-Bromo-2'-deoxyuridine, #B5002), DFO (Deferoxamine mesylate salt, #D9533), G418 (geneticin, Sigma-Aldrich #G418-RO & Gibco #10-131-035), NAC (N-acetyl-l-cysteine, #A9165), PEG 300 (#202371), Propidium iodide (#P4864), RNase A (#R4642), Soybean oil (#S7381), TES ([N-tris-(hydroxymethyl)-methyl-2-aminoethane sulfonic acid], #T1375), Tween-80 (#P1754).

SCD1 inhibitor A939572 (Tocris Bioscience #4845), BODIPY™ 581/591 C11 (Thermo Fisher Scientific, #D3861), Doxycycline HCl (Research Products International Crop. #D43020), MTT (Thiazolyl Blue Tetrazolium Bromide, BIOSYNTH #T-3450), PSVue 643 (Molecular Targeting Technologies P-1006), Puromycin (Gemini Bio Products, #400-128P), Trolox (Calbiochem 648471).

Antibodies

Primary antibodies: Actin (Sigma-Aldrich #A5441 1:10000), 53BP1 (Bethyl #A300-272A, IF 1:2000), COX-2 (PTGS2) (Santa Cruz Biotechnology, Inc. #sc-19999 1:200. FLAG (Sigma-Aldrich #F4049, 1 µg/mL/1:1000), HA (Sigma-Aldrich #H9658, flow cytometry 1:2000), 4-HNE (R&D Systems #MAB3249, flow cytometry 1:100, IF 10 µg/mL/1:100, IHC 20 µg/mL/1:50), NCoR1 (Bethyl #A301-146A, WB 1:1000; Sigma-Aldrich #PLA0170; Bethyl #A301-145A, PLA 10 µg/mL), 8-OHdG (Santa Cruz Biotechnology, Inc. #sc-66036, flow cytometry 1:100, IF 1:100, IHC 1:200), PPARα (Santa Cruz Biotechnology, Inc. #sc-398394, WB 1:500, PLA 1:100), S6K2 (Abcam #ab76960, WB 1:500; Abnova #H00006199-B02P, PLA 2.5 µg/mL), SREBP1 (Thermo Scientific #MS-1207-P0, 1 µg/mL, 1:200), SREBP2 (Abcam #ab30682, 1:500). All other antibodies were purchased from Cell Signaling Technology. Dilution 1:1000, unless otherwise specified. pAkt (T308; #4056),

BrdU (#5292, flow cytometry 1:200), CD31 (PECAM-1) (#77699 IHC 1:100), CD45 (#70257, IHC 1:200), Cleaved Caspase-3 (D175, #9661), pERK (T202/Y204; #4370), p-γH2AX (S139; #9718, flow cytometry 1:400), pMEK (S217/221; #9121), PPARγ (#2443), pRSK (T359/S363; #9344), S6 (#2317), pS6 (S235/236; #4858), pS6 (S240/244; #5364, WB 1:500, flow cytometry 1:100), S6K1 (#2708), pS6K1 (T389; #9234), S6K2 (#14130 WB 1:1000, IP: 1:50, PLA 1:50).

Secondary antibodies: WB: 1:10000. IRDye 680 Conjugated Goat (polyclonal) Anti-Rabbit IgG (H+L) (LI-COR #926-32211). IRDye 800CW Conjugated Goat (polyclonal) Anti-Mouse IgG (H+L) (LI-COR #926-32220). Flow cytometry/IF: 1:500. Alexa Fluor 488 goat anti-rabbit IgG (H+L) (Life technologies #A11008). Alexa Fluor 594 goat anti-rabbit IgG (H+L) (Life technologies #A11012). Alexa Fluor 647 goat anti-rabbit IgG (H+L) (Life technologies #A21244). Alexa Fluor 488 goat anti-mouse IgG (H+L) (Life technologies #A11029). Alexa Fluor 594 goat anti-rabbit IgG (H+L) (Life technologies #A11032).

Plasmids and lentivirus

Packaging plasmids pS-PAX2 and pMD2.G (Addgene) were used to transfect 293T cells and produce lentiviral particles. Melanoma cells were infected with viral particles and selected with the appropriate antibiotics as previously described (Reyes-Uribe et al., 2018). Plasmids: HA-tagged S6K1T389EΔCT in pSLIK inducible vector (G418 selection, 2mg/mL; Addgene #58516). Protein expression was induced with doxycycline (2 µg/mL). Flag-tagged S6K1T389S in pLJM vector (puromycin selection, 2 µg/mL; Addgene #48800), HA-tagged S6K2 wild-type (WT) (Addgene #17729) or S6K2T388E (Addgene#17731) was subcloned into pLUT-poly inducible vector (puromycin selection, 2 µg/mL; gift from Dr. Meenhard Herlyn, The Wistar Institute). S6K1, S6K2 and PPARα short hairpin RNAs in pLKO.1 vector. S6K1 shRNA (sh1: TRCN0000003158, sh4: TRNC0000003161, sh5:

TRNC0000003162). S6K2 shRNA (sh1: TRNC0000000729, sh4: TRNC0000010540, sh5: TRCN0000432273, sh6: TRCN0000199513). PPARα shRNA: (TRCN0000001669). Inducible S6K1 shRNA in TRIPZ lentiviral vector (sh3: V3THS_387795, sh4: V3THS_387797).

siRNA transfection

Melanoma cells ($1x10^6$ cells/10 cm dish) were transfected with 25 nM SREBP1 siRNA (SMARTpool: ON-TARGETplus SREBF1 siRNA #L-006891-00), 25 nM SREBP2 siRNA (SMARTpool: ON-TARGETplus SREBF2 siRNA #L-009549-00), 12.5 nM SREBP1 + 12.5 nM SREBP2 siRNA or 25 nM non-targeting siRNA (ON-TARGETplus Non-targeting Pool #D-001810-10) using DharmaFECT 1 Transfection Reagent (#T-2001; 1:500 final dilution) following the manufacturer instructions for 16h.

Immunoblotting

Cells were lysed with RIPA buffer (50 mM Tris-HCl, pH 7.4, 150 mM NaCl, 1% NP-40, 0.5% sodium deoxycholate, 1 mM EDTA, 2.5 mM sodium pyrophosphate, 0.05% or 0.1% SDS) supplemented with sodium vanadate (0.2 mM) and protease inhibitor cocktail (Sigma-Aldrich #11697498001). Immunoblotting was performed as previously described (Echevarria-Vargas et al., 2018). Immunoblots were imaged with an Odyssey Infrared Imaging System and signal intensity was quantified with Image Studio Lite (LI-COR Biosciences).

Immunostaining

Flow cytometry

Cells were trypsinized, rinsed with PBS, fixed in 90% ice cold EtOH/PBS and stored at -20°C. Cells were washed twice with PBS followed by incubation with 1% BSA/PBS

(incubation buffer) 10 min at room temperature (RT). Cells were incubated with primary antibodies in incubation buffer, 1h at RT and washed once with incubation buffer. Cells were incubated with secondary antibody, 30 min at RT, washed once with incubation buffer, and analyzed by flow cytometry (BD LSRII 14-color flow cytometer analyzer). Data analyses were performed using FlowJo flow software. For 4-HNE staining, cells were fixed with 4% paraformaldehyde for 15 min, washed with PBS and stored at 4°C. Before immunostaining, cells were permeabilized with 0.5% Triton X-100/PBS for 10 min.

Immunofluorescence

Cells were grown on coverslips, fixed with 4% paraformaldehyde for 10 min at RT and permeabilized with 0.2% Triton X-100 for 5 min. Alternatively, cells were fixed and permeabilized with methanol for 10 min at -20°C. Fixed cells were washed twice with PBST (0.1% Tween-20) and blocked with 2% BSA/PBST at RT for 1h. Cells were incubated with primary antibody (in 2% BSA/PBST) overnight at 4°C followed by three washes with PBST. Cells were incubated with secondary antibody (in 2% BSA/PBST) at RT for 1h followed by three washes with PBST. Stained cells were mounted with ProLong Gold antifade reagent with DAPI (Thermo Fisher Scientific #P36935). Fluorescence images were acquired using a Nikon 80i upright microscope.

Immunohistochemistry

Immunohistochemistry was performed by the Wistar Histotechnology Core Facility. Briefly, tumors were fixed with 10% buffered formalin (MedSupply Partners #8BUFF-FORM 10%), embedded in paraffin and cut into 4 µm consecutive sections. Deparaffinized sections were steamed in citrate buffer (pH 6) for 20 min or incubated in pressure cooker with DAKO EDTA (pH9, Agilent Dako #S2367) for 20 min to retrieve antigens. Samples were treated

with 3% H_2O_2 solution for 10 min and then Triton X-100 (0.3% in PBS) for 15 min at RT. Samples were blocked with 5% horse serum in PBS for 1h at RT, incubated with primary antibodies (4-HNE 1:50, 8-OHdG 1:200, CD31 1:100 or CD45 1:200 in 4% BSA/PBS) overnight at 4°C, and incubated with secondary antibodies for 30 min at RT. All wash steps were performed with 0.5% PBST. Antigens were detected using diaminobenzidine (DAB). Slides were counterstained with hematoxylin. IHC images were acquired using a Nikon 80i upright microscope.

Immunoprecipitation

3 x 10^6 cells were cultured for approximately 36 h, harvested by trypsin-EDTA and lysed in 50 mM Tris-HCl pH 7.4, 150 mM NaCl, 1% Triton X100, 1 mM EDTA, 2.5 mM sodium pyrophosphate, 1 mM sodium vanadate, protease inhibitor cocktail (Sigma-Aldrich #11697498001). Proteins (2 mg/500 µl) were pre-cleared by incubating with protein G sepharose beads (Sigma-Aldrich #P3296; blocked with 0.1% BSA prior to the incubation) at 4°C for 3h. Supernatants were then incubated with IgG (1 µg, Sigma-Aldrich #I8140) or S6K2 antibody (Cell signaling #14130 1:50) overnight at 4°C. Immuno-complexes were captured by incubating with 0.1% BSA blocked protein G beads for 3h at 4°C. Immunoprecipitates were eluted with 1.5X sample buffer (NuPAGE LDS Sample Buffer, Invitrogen #NP0007) with 1.5% 2-ME at 95°C for 5 min.

Proximity ligation assay

Cells were grown on chamber slides (Lab-Tek II #154534), fixed with 4% paraformaldehyde for 10 min and washed three times with PBS. Proximity ligation assay was performed using Duolink In Situ Red Starter Kit Mouse/Rabbit (Sigma-Aldrich #DUO92101) per the manufacturer's instructions. Briefly, cells were incubated with

blocking solution for 60 min at 37°C, primary antibodies overnight at 4°C, and PLA probe solution for 60 min at 37°C in a humidity chamber. Following primary antibody and probe incubations, cells were washed two times with wash buffer A for 5 min. Cells were then incubated with ligation solution for 30 min at 37°C in a humidity chamber and washed twice with wash buffer A. The ligated probes were amplified by incubating the slides with amplification solution for 100 min at 37°C. Cells were then washed two times with wash buffer B for 10 min and one time with 1% wash buffer B for 1 min. Slides were mounted and analyzed on a Leica TCS SP5 II scanning spectral confocal microscope.

Subcellular fractionation

Subcellular protein fractionation was performed per the manufacturer's instructions (Subcellular Protein Fractionation Kit for Cultured Cells; Thermo Scientific #78840). Briefly, 2 x 10^6 cells were harvested by trypsin-EDTA and washed with PBS. Cytoplasmic, membrane or nuclear proteins were sequentially extracted by CEB, MEB or NEB buffer (200: 200: 100 µl) containing protease inhibitors at 4°C, incubation time: 10, 10 and 30 min respectively. Chromatin-bound proteins were isolated by incubating the insoluble fraction of nuclear proteins with 100 µl NEB containing 5 mM CaCl2, 3 units/µl micrococcal nuclease and protease inhibitors at RT for 15 min. Supernatants from each step were analyzed by SDS-PAGE.

qRT-PCR

RNA was extracted with PureLink RNA mini kit (Thermo Fisher Scientific, Invitrogen™ #12183018A). Cell pellets were homogenized using QIAshredder (QIagen #79656) before RNA extraction. DNA was removed by On-column PureLink DNase treatment (Thermo Fisher Scientific, Invitrogen™ #12185010). First-strand cDNA was synthesized using

Maxima cDNA kit (Thermo Scientific™ #K1642). Real time qPCR was performed using SYBR green PCR Master Mix (Applied Biosystems #4385612). Tumor samples were preserved in RNAlater solution (Invitrogen #AM7020) and stored at 4°C. Tumors were chopped into small pieces. RNA extraction, cDNA synthesis and RT-qPCR were performed as cell pellets.

Cell viability assays

MTT assay

Cells were seeded in 96-well plates (2500 cells/well) and treated with drugs by adding 2X compounds (prepared in fresh growth medium) to the cells. After 72h, cell viability was determined by standard MTT Assays. Absorbance was determined at 490 nm using a BioTek plate reader.

CellTiter-Glo assay

Cells were seeded in 384-well plates (500 cells/well) and treated with drugs using the Janus MDT Nanohead. After 72h, the medium was removed and cell viability was measured using CellTiter-Glo (Promega). Data were normalized where 100% viability equals to luminescence of DMSO-treated cells, and 0% viability equals to luminescence of 1 μM bortezomib-treated cells.

Cell proliferation assay

Colorimetric detection

BrdU incorporation was performed per the manufacturer's instructions (BrdU Cell Proliferation Assay Kit; Cell Signaling Technology #6813). Briefly, cells were seeded in 96-well plates (2500 cells/well) one day before drug treatment. Cells were treated with drugs

for 72 h, followed by BrdU labelling for 16h and 30 min incubation in fixing/denaturing solution at RT. Cells were then incubated with primary antibody for 1h at RT, washed three times followed by incubation with HRP-conjugated antibody solution at RT for 30 min. Colorimetric reactions for BrdU incorporation were started by incubation with TMB substrate (10 min at RT) and terminated by adding STOP solution; signal was determined by absorbance at 450 nm.

BrdU/PI double staining

Cells were labeled with BrdU (10 μM) for 4h, trypsinized and fixed with cold 70% EtOH/PBS. Fixed cells were rinsed with PBS and incubated with 1.5 M HCl for 30 min at RT. Cells were then washed twice with PBS and twice with incubation buffer (IB, 0.5% BSA in PBS). Cells were blocked with IB for 10 min at RT before incubating with BrdU antibody (CST 1:200) for 1h at RT and with secondary antibody for 30 min at RT. Cells were rinsed with IB after each antibody incubation. Cells were incubated with PI (40 μg/mL)/RNase A (1 μg/mL) in PBS for 5 min before assessing DNA content and BrdU incorporation by flow cytometry.

Cell death assay

Floating and attached cells were harvested, rinsed with TES [N-tris-(hydroxymethyl)-methyl-2-aminoethane sulfonic acid] buffer (5 mM TES, 145 mM NaCl, pH 7.4) and incubated in PSVue 643/TES (3 μM; Molecular Targeting Technologies, Inc. #P-1006) for 10 min at RT. Cells were rinsed with TES buffer, resuspend in PI (5 μg/mL)/TES and analyzed on a flow cytometer (LSRII 14color analyzer, BD Biosciences).

Measurement of ROS production

Cells were trypsinized, washed with PBS and incubated with H2DCFDA [2',7'-dichlorodihydrofluorescein diacetate, Thermo Fisher Scientific] (10 μM in PBS) for 25 min at 37°C. Cells were then washed once with PBS to remove the dye and incubated in phenol red free growth medium for 10 min at 37°C. Following incubation, cells were placed on ice, protected from light and immediately analyzed by flow cytometry.

Lipid peroxidation measurement

Cells were harvested and incubated with Bodipy 581/591 C11 (5 μM in growth medium; Thermo Fisher Scientific) for 30 min at 37°C. Cells were washed 5 times with PBS and then analyzed by flow cytometry.

Proteomics

Sample preparation and LC-MS/MS analysis

M93-047 cells transduced with vector control, S6K1 shRNA (sh1/4 or sh5) or S6K2 shRNA (sh1 or sh4) were cultured in 6 cm plates. Four days post-transduction, cells were washed twice with ice-cold Hank's Balanced Salt Solution and lysed with SDS buffer (50 mM Tris-HCl pH 7.5, 150 mM NaCl, 1% SDS and 1 mM EDTA) supplemented with protease inhibitors (150 μM PMSF, 1 μg/mL Pepstatin A and 1 μg/mL Leupeptin). In-gel trypsin digestion was performed using 15 μg of lysate from triplicate samples as described previously (Beer et al., 2011).

LC-MS/MS of peptides was performed using a Waters nanoACQUITY UPLC in-line with a Thermo Q Exactive Plus mass spectrometer. For each sample, 1 μg of tryptic digest was loaded onto a 180 μm x 2 cm nanoACQUITY UPLC Symmetry C18 trap column with 5 μm particle size (Waters #186006527) followed by analytical separation on a 1.7 μm x 2.5 cm ACQUITY UPLC Peptide BEH C18 column with 1.7 μm particle size (Waters #186003546).

Samples were analyzed in data-dependent mode using a 245 min LC gradient with water (solvent A) and acetonitrile (solvent B) containing 0.1% formic acid: 5-30% B over 225 min, 30-80% B over 5 min, 80% B hold for 10 min and return to initial conditions for 5 min. Full MS spectra were recorded at a resolution of 70,000 using a 400-2000 m/z scan range. Data-dependent MS/MS was performed on the top 20 most abundant ions selected with an isolation width of 1.5 m/z and were recorded at a resolution of 17,500.

Data analysis

RAW files were processed using MaxQuant 1.5.1.2 in a single run (Cox and Mann, 2008). Database searches were performed against the UniProt human sequence database (June 29, 2017; 159,819 sequences) and an in-house database of common laboratory contaminants (July 28, 2014; 3,671 sequences) with Trypsin/P specificity, a maximum of 2 missed cleavages and a minimum peptide length of 7 residues. Precursor and fragment mass tolerances were set to 4.5 ppm and 20 ppm, respectively. Protein N-terminal acetylation and methionine oxidation were set as variable modifications. Cysteine carbamidomethylation was set as a fixed modification. A maximum of 5 modifications were allowed per peptide. Peptide and protein false discovery rates were both set to 1%. Match between runs was enabled with a 0.7 min match time window and 20 min alignment time window. Protein quantification was based on unique peptides only. Label-free protein quantitation (LFQ) to normalize between samples was performed with a minimum peptide ratio of 1. Statistical analysis was performed using Perseus 1.5.0.31 (Tyanova et al., 2016). Protein groups identified by a single unique peptide or corresponding to contaminants were removed. LFQ intensities were log2 transformed to reduce outlier effects, and missing values were imputed from a downshifted normal distribution. Statistical significance between conditions after pooling data from the two different shRNAs for the same S6K was defined as Student's t-test p-value less than 0.05 and absolute fold-change greater than 2

based on log2-transformed LFQ intensities. Where indicated, correction for multiple testing was performed by permutation-based false discovery rate (FDR). Canonical pathway analysis was performed using QIAGEN's Ingenuity® Pathway Analysis software (IPA®, QIAGEN Redwood City,www.qiagen.com/ingenuity) with all identified proteins as the reference dataset.

Lipidomics

Sample preparation and LC-MS/MS analysis

M93-047 cells were transduced with vector control, S6K1 shRNA or S6K2 shRNA. Four days post transduction, lipids were extracted from cells grown in 10 cm plates using a modified Folch method (Folch et al., 1957). Briefly, media was removed from the plates and the cells were washed twice with PBS. Cells were quenched with ice-cold MeOH and transferred to a glass tube. Splash (Avanti Polar Lipids #330707) internal standard was added to each sample. Ice-cold 0.88% NaCl in water and $CHCl_3$ were added to a final ratio of 2:1:1 $CHCl_3$:MeOH:0.88% NaCl. Extracts were then sonicated and centrifuged. The lower organic phase was transferred to a new glass tube. The upper aqueous phase was re-extracted with synthetic organic phase, and the re-extracted organic phase was pooled with the initial extract. The pooled organic phases were dried under nitrogen, and lipids were reconstituted in 1:8:1 $CHCl_3$:MeOH:H_2O. Global lipid extracts from triplicate plates were analyzed by reversed-phase LC-MS/MS on a Thermo Q Exactive HF-X in both positive and negative polarities. For each polarity, 1% (2 µL) of the resuspended lipidome was loaded onto a 150 µm x 2.1 cm Accucore C30 column with a 2.6 µm particle size (Thermo Fisher Scientific #27826-152130). The lipidome was analyzed using data-dependent acquisition on a 40 minute gradient with 1:1 acetonitrile:water with 5 mM

ammonium formate and 0.1% formic acid (solvent A) and 88:10:2 isopropanol:acetonitrile:water with 5 mM ammonium formate and 0.1% formic acid (solvent B). The gradient is as follows: 0-60% B over 10 minutes, 60-85% B over 10 minutes, 85-100% over 10 minutes and holding for 5 minutes and re-equilibrating to initial conditions over 5 minutes. Full MS spectra were recorded at a resolution of 120,000 using a 300-1,200 m/z scan range in positive mode and 250-1,200 m/z scan range in negative mode. Data-dependent MS/MS scans were recorded at a resolution of 15,000 for the top 20 most abundant ions isolated with a 0.4 m/z isolation width. Stepped collision energy (NCE) of 20/30 was used in positive mode and 20/30/40 was used in negative mode.

Data analysis

Quantitation for global lipids was performed using Lipid Search 4.1 (Thermo Fisher Scientific). Briefly, raw files were processed using Lipid Search software in a single batch. Lipids were identified based on mass, retention time and predicted fragmentation patterns. All identified lipids are aligned and quantified with a 5 ppm mass tolerance and a retention time window of 0.2 minutes. Manual filtering included removing low scoring lipid identifications and unlikely adducts based on standards. To quantify lipid distribution, the abundance (peak area) of each lipid species in a sample was normalized to total lipid peak area in that sample. Statistical significance was defined as a Student's t-test p-value less than 0.05.

RNA seq

Sample preparation

Cells were lysed in Tri-Reagent (Sigma-Aldrich, #T9424-100ml) and RNA was extracted using the Direct-zol MiniPrep Kit (Zymo Research, #R2050) with in column DNAse I treatment. Quality of RNA was checked using the TapeStation 4200 High Sensitivity RNA

ScreenTape (Agilent Technologies, #5067-5576) and concentration was determined using the Qubit 2.0 Fluorometer (ThermoFisher Scientific). Total RNA (200ng) was used to prepare 3' QuantSeq mRNASeq libraries (Lexogen, #KO152x96) as per protocol. Fourteen PCR cycles were used for amplification during the library preparation. Libraries were checked for quality using the TapeStation High Sensitivity D5000 ScreenTape (Agilent Technologies, #5067-5592). Quantitation of library was done using qPCR (Roche #KK4835). Sequencing was done on the NextSeq 500 (Illumina) per manufacturer's instructions using a 75 cycle High Output sequencing kit. A final concentration of 1.9pM was loaded onto the flowcell.

Data analysis

RNA-seq data was aligned using *bowtie2* (Langmead and Salzberg, 2012) against hg19 version of the human genome and *RSEM* v1.2.12 software (Li and Dewey, 2011) was used to estimate raw read counts and RPKM using Ensemble transcriptome. *DESeq2* (Love et al., 2014) was used to estimate significance of differential expression between each shRNA and control condition. Genes with expression changes passing FDR<5% threshold were considered significant. Only genes that overlapped between the two shRNAs for S6K1 (sh1/4 and sh5) or S6K2 (sh1 and sh4) were analyzed. Heatmaps were normalized by DESeq2 log2 scaled counts relative to average across all samples. Gene set enrichment analysis was done using QIAGEN's Ingenuity® Pathway Analysis software (IPA®, QIAGEN Redwood City,www.qiagen.com/ingenuity) and significance of enrichment for Upstream Regulators was defined at p-value<0.05.

Reverse phase protein array

Sample preparation

RPPA was performed by the MD Anderson Center RPPA core facility as previous described (Tibes et al., 2006). Cells were lysed with 1% Triton X-100, 50 mM HEPES, pH7.4, 150 mM NaCl, 1.5 mM $MgCl_2$, 1 mM EGTA, 100 mM NaF, 10 mM Sodium pyrophosphate, 1 mM sodium vanadate, 10% glycerol, protease and phosphatase cocktail (Sigma-Aldrich #11873580001 and 04906837001). Lysates were mixed with sample buffer (10% glycerol, 2% SDS, 0.06 M Tris-HCl, pH 6.8, 1/40 volume of β-mercaptoethanol) and boiled. Samples were printed on nitrocellulose-coated slides, probed with 200-300 validated primary antibodies. Signals were detected by 3,3-diaminobenzidine (DAB) colorimetric reaction, scanned, analyzed, and quantified using Array-Pro Analyzer software (MediaCybernetics).

Data analysis

For MAPKi-treated cells, ratio in protein expression was calculated relative to vehicle-treated cells. Ratios were converted to fold change values: fold change = ratio when ratio >1 and fold change = -1/ratio for ratio <1. Fold changes are depicted in the heatmap with positive values indicating upregulation in MAPKi-treated cells (red, fold change >0) and negative values indicate downregulation (blue, fold change <-1). White squares denote samples where fold change values were below the threshold (±1.2). Mixed-effect model was used to examine the difference of the measured outcome between resistant cell lines vs. sensitive cell lines.

For cells transduced with S6K shRNA, protein levels were transformed to log2 and fold changes were calculated relative to vector-transduced cells. Heatmaps depict average values of 2 shRNA hairpins. Significance of effect differences between S6K1sh vs. S6K2sh was estimated using paired t-test on expression differences vs. Vec at different cell lines, days, shRNAs and replicates.

Analysis of publicly available dataset

TCGA data, S6K1 and S6K2 correlation and survival

To determine the relationship between S6K2 and S6K1 in melanoma, a correlation plot was generated using R2: Genomics Analysis and Visualization Platform (http://r2.amc.nl). Log2-transformed expression values of S6K1 and S6K2 mRNA expression from 470 human melanoma patient tumors from the TCGA Skin Cutaneous Melanoma dataset (SKCM) were used for the analysis.

Kaplan–Meier survival curves for S6K1 and S6K2 expression in melanoma patients treated with targeted therapies (Vemurafenib, Dabrafenib, Trametinib) as one of their treatments (N=355 melanoma patients), were obtained using the TCGA skin cutaneous melanoma dataset. The analysis was performed using R2: Genomics Analysis and Visualization Platform (http://r2.amc.nl). Average gene expression was considered, and P values were obtained from log-rank tests comparing the two Kaplan–Meier curves.

Analysis of animal studies

To compare tumor volume at end of follow-up among experimental groups, ANOVA testing with post-hoc pairwise t-tests were performed, and FDR adjusted p-values are reported. For the analysis of longitudinal data from *in vivo* tumor growth experiments, linear mixed effects models were applied to compare tumor growth rates between treatment groups. For multiple comparisons, FDR adjusted P-value <0.05 was considered significant.

QUANTIFICATION AND STATISTICAL ANALYSIS

Data were analyzed and plotted using GraphPad Prism 5 software or Microsoft Excel. Data are presented as mean ± SD or mean ± SEM as indicated in each figure legend; replicate

numbers (n) are indicated in the figure legends. In graphs showing mean of multiple independent experiments, values of technical replicates were first averaged to represent each experiment, and n denotes how many independent experiments were performed. In graphs showing one representative experiment, n denotes number of technical replicates.

Figs. 6C and S6C. M93-047 and WM4023 (PDX): Bar graphs show mean ± SEM of two representative fields from a representative tumor. WM1366 and WM3623: Bar graphs show mean ± SEM of 3 to 4 tumors in each treatment group. Each tumor was represented by average of 2 to 5 representative fields.

Fig. S6E. M93-047: CD31 and CD45, bar graphs show mean ± SEM of 3 to 4 tumors in each treatment group. Each tumor was represented by average of 2 to 5 representative fields.

WM1366: CD31, bar graphs show mean ± SEM of 2 to 3 representative fields. CD45, bar graphs show mean ± SEM of 3 to 4 tumors in each treatment group. Each tumor was represented by average of 3 representative fields.

Statistical differences between two experimental groups were calculated using the unpaired two-tailed Student's t-test, unless otherwise specified.

Fig. 1A. Mixed-effects modeling was used to examine the difference of the measured outcome between resistant cell lines versus sensitive cell lines.

Fig. 2G. The measurement of ROS and lipid peroxidation were first rescaled as fold change from its corresponding control in Vec group. Two-group t-test was used to compare the average fold-change of ROS (or lipid peroxidation) between MAPKi-R versus MAPKi-S upon S6K1 or S6K2 depletion. Bonferroni's adjusted p-values were reported.

A significance level of *$p < 0.05$, **$p < 0.01$ and ***$p < 0.001$ was used throughout the study

(except Figures 1B and S1K, where a significance level of *p < 0.01, **p < 0.001 and ***p < 0.0001 was used, if the thresholds were used instead of numbers).

DATA AND SOFTWARE AVAILABILITY

Proteomics dataset generated from M93-047 cell line has been deposited to the MassIVE repository (accession # MSV000083480).

https://massive.ucsd.edu/ProteoSAFe/dataset.jsp?task=e702a8018b224a52a737ee2ba323b3a4

RNA-seq dataset generated from M93-047 cell line has been deposited into the Gene Expression Omnibus (GEO) repository (accession #GSE127916).

https://www.ncbi.nlm.nih.gov/geo/query/acc.cgi?acc=GSE127916

REFERENCES

Aitken, R. J., Whiting, S., De Iuliis, G. N., McClymont, S., Mitchell, L. A., and Baker, M. A. (2012). Electrophilic aldehydes generated by sperm metabolism activate mitochondrial reactive oxygen species generation and apoptosis by targeting succinate dehydrogenase. J Biol Chem *287*, 33048-33060.

Ascierto, P. A., Schadendorf, D., Berking, C., Agarwala, S. S., van Herpen, C. M., Queirolo, P., Blank, C. U., Hauschild, A., Beck, J. T., St-Pierre, A.*, et al.* (2013). MEK162 for patients with advanced melanoma harbouring NRAS or Val600 BRAF mutations: a non-randomised, open-label phase 2 study. Lancet Oncol *14*, 249-256.

Atefi, M., von Euw, E., Attar, N., Ng, C., Chu, C., Guo, D., Nazarian, R., Chmielowski, B., Glaspy, J. A., Comin-Anduix, B.*, et al.* (2011). Reversing melanoma cross-resistance to BRAF and MEK inhibitors by co-targeting the AKT/mTOR pathway. PLoS One *6*, e28973.

Ayala, A., Munoz, M. F., and Arguelles, S. (2014). Lipid peroxidation: production, metabolism, and signaling mechanisms of malondialdehyde and 4-hydroxy-2-nonenal. Oxid Med Cell Longev *2014*, 360438.

Bankhead, P., Loughrey, M. B., Fernandez, J. A., Dombrowski, Y., McArt, D. G., Dunne, P. D., McQuaid, S., Gray, R. T., Murray, L. J., Coleman, H. G.*, et al.* (2017). QuPath: Open source software for digital pathology image analysis. Sci Rep *7*, 16878.

Barclay, L. R., Artz, J. D., and Mowat, J. J. (1995). Partitioning and antioxidant action of the water-soluble antioxidant, Trolox, between the aqueous and lipid phases of phosphatidylcholine membranes: 14C tracer and product studies. Biochim Biophys Acta *1237*, 77-85.

Beer, L. A., Tang, H. Y., Sriswasdi, S., Barnhart, K. T., and Speicher, D. W. (2011). Systematic discovery of ectopic pregnancy serum biomarkers using 3-D protein profiling coupled with label-free quantitation. J Proteome Res *10*, 1126-1138.

Burd, C. E., Liu, W., Huynh, M. V., Waqas, M. A., Gillahan, J. E., Clark, K. S., Fu, K., Martin, B. L., Jeck, W. R., Souroullas, G. P.*, et al.* (2014). Mutation-specific RAS oncogenicity explains NRAS codon 61 selection in melanoma. Cancer Discov *4*, 1418-1429.

Canli, O., Alankus, Y. B., Grootjans, S., Vegi, N., Hultner, L., Hoppe, P. S., Schroeder, T., Vandenabeele, P., Bornkamm, G. W., and Greten, F. R. (2016). Glutathione peroxidase 4 prevents necroptosis in mouse erythroid precursors. Blood *127*, 139-148.

Corcoran, R. B., Rothenberg, S. M., Hata, A. N., Faber, A. C., Piris, A., Nazarian, R. M., Brown, R. D., Godfrey, J. T., Winokur, D., Walsh, J.*, et al.* (2013). TORC1 suppression predicts responsiveness to RAF and MEK inhibition in BRAF-mutant melanoma. Sci Transl Med *5*, 196ra198.

Cox, J., and Mann, M. (2008). MaxQuant enables high peptide identification rates, individualized p.p.b.-range mass accuracies and proteome-wide protein quantification. Nat Biotechnol *26*, 1367-1372.

Dawson, M. I., and Xia, Z. (2012). The retinoid X receptors and their ligands. Biochim Biophys Acta *1821*, 21-56.

Dixon, S. J., Lemberg, K. M., Lamprecht, M. R., Skouta, R., Zaitsev, E. M., Gleason, C. E., Patel, D. N., Bauer, A. J., Cantley, A. M., Yang, W. S.*, et al.* (2012). Ferroptosis: an iron-dependent form of nonapoptotic cell death. Cell *149*, 1060-1072.

Dummer, R., Schadendorf, D., Ascierto, P. A., Arance, A., Dutriaux, C., Di Giacomo, A. M., Rutkowski, P., Del Vecchio, M., Gutzmer, R., Mandala, M.*, et al.* (2017). Binimetinib versus dacarbazine in patients with advanced NRAS-mutant melanoma (NEMO): a multicentre, open-label, randomised, phase 3 trial. Lancet Oncol *18*, 435-445.

Duvel, K., Yecies, J. L., Menon, S., Raman, P., Lipovsky, A. I., Souza, A. L., Triantafellow, E., Ma, Q., Gorski, R., Cleaver, S.*, et al.* (2010). Activation of a metabolic gene regulatory network downstream of mTOR complex 1. Mol Cell *39*, 171-183.

Echevarria-Vargas, I. M., Reyes-Uribe, P. I., Guterres, A. N., Yin, X., Kossenkov, A. V., Liu, Q., Zhang, G., Krepler, C., Cheng, C., Wei, Z.*, et al.* (2018). Co-targeting BET and MEK as salvage therapy for MAPK and checkpoint inhibitor-resistant melanoma. EMBO Mol Med *10*.

Eroglu, Z., Holmen, S. L., Chen, Q., Khushalani, N. I., Amaravadi, R., Thomas, R., Ahmed, K. A., Tawbi, H., Chandra, S., Markowitz, J.*, et al.* (2019). Melanoma central nervous system metastases: An update to approaches, challenges, and opportunities. Pigment Cell Melanoma Res *32*, 458-469.

Fattore, L., Marra, E., Pisanu, M. E., Noto, A., de Vitis, C., Belleudi, F., Aurisicchio, L., Mancini, R., Torrisi, M. R., Ascierto, P. A., and Ciliberto, G. (2013). Activation of an early feedback survival loop involving phospho-ErbB3 is a general response of melanoma cells to RAF/MEK inhibition and is abrogated by anti-ErbB3 antibodies. J Transl Med *11*, 180.

Folch, J., Lees, M., and Sloane Stanley, G. H. (1957). A simple method for the isolation and purification of total lipides from animal tissues. J Biol Chem *226*, 497-509.

Friedmann Angeli, J. P., Schneider, M., Proneth, B., Tyurina, Y. Y., Tyurin, V. A., Hammond, V. J., Herbach, N., Aichler, M., Walch, A., Eggenhofer, E.*, et al.* (2014). Inactivation of the ferroptosis regulator Gpx4 triggers acute renal failure in mice. Nat Cell Biol *16*, 1180-1191.

Gopal, Y. N., Deng, W., Woodman, S. E., Komurov, K., Ram, P., Smith, P. D., and Davies, M. A. (2010). Basal and treatment-induced activation of AKT mediates resistance to cell death by AZD6244 (ARRY-142886) in Braf-mutant human cutaneous melanoma cells. Cancer Res *70*, 8736-8747.

Green, D. R. (2019). The Coming Decade of Cell Death Research: Five Riddles. Cell *177*, 1094-1107.

Griffiths, B., Lewis, C. A., Bensaad, K., Ros, S., Zhang, Q., Ferber, E. C., Konisti, S., Peck, B., Miess, H., East, P.*, et al.* (2013). Sterol regulatory element binding protein-dependent regulation of lipid synthesis supports cell survival and tumor growth. Cancer Metab *1*, 3.

Hagen, R. M., Rodriguez-Cuenca, S., and Vidal-Puig, A. (2010). An allostatic control of membrane lipid composition by SREBP1. FEBS Lett *584*, 2689-2698.

Hangauer, M. J., Viswanathan, V. S., Ryan, M. J., Bole, D., Eaton, J. K., Matov, A., Galeas, J., Dhruv, H. D., Berens, M. E., Schreiber, S. L.*, et al.* (2017). Drug-tolerant persister cancer cells are vulnerable to GPX4 inhibition. Nature *551*, 247-250.

Hayward, N. K., Wilmott, J. S., Waddell, N., Johansson, P. A., Field, M. A., Nones, K., Patch, A. M., Kakavand, H., Alexandrov, L. B., Burke, H.*, et al.* (2017). Whole-genome landscapes of major melanoma subtypes. Nature *545*, 175-180.

Hollebecque, A., Houede, N., Cohen, E. E., Massard, C., Italiano, A., Westwood, P., Bumgardner, W., Miller, J., Brail, L. H., Benhadji, K. A., and Soria, J. C. (2014). A phase Ib trial of LY2584702 tosylate, a p70 S6 inhibitor, in combination with erlotinib or everolimus in patients with solid tumours. Eur J Cancer *50*, 876-884.

Jeon, T. I., and Osborne, T. F. (2012). SREBPs: metabolic integrators in physiology and metabolism. Trends Endocrinol Metab *23*, 65-72.

Juric, D., Soria, J.-C., Sharma, S., Banerji, U., Azaro, A., Desai, J., Ringeisen, F. P., Kaag, A., Radhakrishnan, R., Hourcade-Potelleret, F.*, et al.* (2014). A phase 1b dose-escalation study of BYL719 plus binimetinib (MEK162) in patients with selected advanced solid tumors. Journal of Clinical Oncology *32*, 9051.

Kagan, V. E., Mao, G., Qu, F., Angeli, J. P., Doll, S., Croix, C. S., Dar, H. H., Liu, B., Tyurin, V. A., Ritov, V. B.*, et al.* (2017). Oxidized arachidonic and adrenic PEs navigate cells to ferroptosis. Nat Chem Biol *13*, 81-90.

Kang, S. A., Pacold, M. E., Cervantes, C. L., Lim, D., Lou, H. J., Ottina, K., Gray, N. S., Turk, B. E., Yaffe, M. B., and Sabatini, D. M. (2013). mTORC1 phosphorylation sites encode their sensitivity to starvation and rapamycin. Science *341*, 1236566.

Karlsson, E., Magic, I., Bostner, J., Dyrager, C., Lysholm, F., Hallbeck, A. L., Stal, O., and Lundstrom, P. (2015). Revealing Different Roles of the mTOR-Targets S6K1 and S6K2 in Breast Cancer by Expression Profiling and Structural Analysis. PLoS One *10*, e0145013.

Kersten, S. (2014). Integrated physiology and systems biology of PPARalpha. Mol Metab *3*, 354-371.

Kim, K., Pyo, S., and Um, S. H. (2012). S6 kinase 2 deficiency enhances ketone body production and increases peroxisome proliferator-activated receptor alpha activity in the liver. Hepatology *55*, 1727-1737.

Koster, J., Volckmann, R., Zwijnenburg, D., Molenaar, P., and Versteeg, R. (2019). R2: Genomics analysis and visualization platform. Cancer Res *79*, Abstract nr 2490.

Koundouros, N., and Poulogiannis, G. (2020). Reprogramming of fatty acid metabolism in cancer. Br J Cancer *122*, 4-22.

Langmead, B., and Salzberg, S. L. (2012). Fast gapped-read alignment with Bowtie 2. Nat Methods *9*, 357-359.

Lee, G., Zheng, Y., Cho, S., Jang, C., England, C., Dempsey, J. M., Yu, Y., Liu, X., He, L., Cavaliere, P. M.*, et al.* (2017). Post-transcriptional Regulation of De Novo Lipogenesis by mTORC1-S6K1-SRPK2 Signaling. Cell *171*, 1545-1558 e1518.

Lee-Fruman, K. K., Kuo, C. J., Lippincott, J., Terada, N., and Blenis, J. (1999). Characterization of S6K2, a novel kinase homologous to S6K1. Oncogene *18*, 5108-5114.

Lefterova, M. I., Zhang, Y., Steger, D. J., Schupp, M., Schug, J., Cristancho, A., Feng, D., Zhuo, D., Stoeckert, C. J., Jr., Liu, X. S., and Lazar, M. A. (2008). PPARgamma and C/EBP factors orchestrate adipocyte biology via adjacent binding on a genome-wide scale. Genes Dev *22*, 2941-2952.

Li, B., and Dewey, C. N. (2011). RSEM: accurate transcript quantification from RNA-Seq data with or without a reference genome. BMC Bioinformatics *12*, 323.

Love, M. I., Huber, W., and Anders, S. (2014). Moderated estimation of fold change and dispersion for RNA-seq data with DESeq2. Genome Biol *15*, 550.

Magnuson, B., Ekim, B., and Fingar, D. C. (2012). Regulation and function of ribosomal protein S6 kinase (S6K) within mTOR signalling networks. Biochem J *441*, 1-21.

Magtanong, L., Ko, P. J., and Dixon, S. J. (2016). Emerging roles for lipids in non-apoptotic cell death. Cell Death Differ *23*, 1099-1109.

Nardella, C., Lunardi, A., Fedele, G., Clohessy, J. G., Alimonti, A., Kozma, S. C., Thomas, G., Loda, M., and Pandolfi, P. P. (2011). Differential expression of S6K2 dictates tissue-specific requirement for S6K1 in mediating aberrant mTORC1 signaling and tumorigenesis. Cancer Res *71*, 3669-3675.

Nielsen, R., Pedersen, T. A., Hagenbeek, D., Moulos, P., Siersbaek, R., Megens, E., Denissov, S., Borgesen, M., Francoijs, K. J., Mandrup, S., and Stunnenberg, H. G. (2008). Genome-wide profiling of PPARgamma:RXR and RNA polymerase II occupancy reveals temporal activation of distinct metabolic pathways and changes in RXR dimer composition during adipogenesis. Genes Dev *22*, 2953-2967.

Owen, J. L., Zhang, Y., Bae, S. H., Farooqi, M. S., Liang, G., Hammer, R. E., Goldstein, J. L., and Brown, M. S. (2012). Insulin stimulation of SREBP-1c processing in transgenic rat hepatocytes requires p70 S6-kinase. Proc Natl Acad Sci U S A *109*, 16184-16189.

Panigrahy, D., Kaipainen, A., Huang, S., Butterfield, C. E., Barnes, C. M., Fannon, M., Laforme, A. M., Chaponis, D. M., Folkman, J., and Kieran, M. W. (2008). PPARalpha agonist fenofibrate suppresses tumor growth through direct and indirect angiogenesis inhibition. Proc Natl Acad Sci U S A *105*, 985-990.

Pardo, O. E., and Seckl, M. J. (2013). S6K2: The Neglected S6 Kinase Family Member. Front Oncol *3*, 191.

Pavan, I. C., Yokoo, S., Granato, D. C., Meneguello, L., Carnielli, C. M., Tavares, M. R., do Amaral, C. L., de Freitas, L. B., Paes Leme, A. F., Luchessi, A. D., and Simabuco, F. M. (2016). Different interactomes for p70-S6K1 and p54-S6K2 revealed by proteomic analysis. Proteomics *16*, 2650-2666.

Pearce, L. R., Alton, G. R., Richter, D. T., Kath, J. C., Lingardo, L., Chapman, J., Hwang, C., and Alessi, D. R. (2010). Characterization of PF-4708671, a novel and highly specific inhibitor of p70 ribosomal S6 kinase (S6K1). Biochem J *431*, 245-255.

Pende, M., Um, S. H., Mieulet, V., Sticker, M., Goss, V. L., Mestan, J., Mueller, M., Fumagalli, S., Kozma, S. C., and Thomas, G. (2004). S6K1(-/-)/S6K2(-/-) mice exhibit perinatal lethality and rapamycin-sensitive 5'-terminal oligopyrimidine mRNA translation and reveal a mitogen-activated protein kinase-dependent S6 kinase pathway. Mol Cell Biol *24*, 3112-3124.

Pineda Torra, I., Jamshidi, Y., Flavell, D. M., Fruchart, J. C., and Staels, B. (2002). Characterization of the human PPARalpha promoter: identification of a functional nuclear receptor response element. Mol Endocrinol *16*, 1013-1028.

Posch, C., Moslehi, H., Feeney, L., Green, G. A., Ebaee, A., Feichtenschlager, V., Chong, K., Peng, L., Dimon, M. T., Phillips, T.*, et al.* (2013). Combined targeting of MEK and PI3K/mTOR effector pathways is necessary to effectively inhibit NRAS mutant melanoma in vitro and in vivo. Proc Natl Acad Sci U S A *110*, 4015-4020.

Posch, C., Vujic, I., Monshi, B., Sanlorenzo, M., Weihsengruber, F., Rappersberger, K., and Ortiz-Urda, S. (2016). Searching for the Chokehold of NRAS Mutant Melanoma. J Invest Dermatol *136*, 1330-1336.

Rakhshandehroo, M., Knoch, B., Muller, M., and Kersten, S. (2010). Peroxisome proliferator-activated receptor alpha target genes. PPAR Res *2010*.

Rees, M. G., Seashore-Ludlow, B., Cheah, J. H., Adams, D. J., Price, E. V., Gill, S., Javaid, S., Coletti, M. E., Jones, V. L., Bodycombe, N. E.*, et al.* (2016). Correlating chemical sensitivity and basal gene expression reveals mechanism of action. Nat Chem Biol *12*, 109-116.

Reyes-Uribe, P., Adrianzen-Ruesta, M. P., Deng, Z., Echevarria-Vargas, I., Mender, I., Saheb, S., Liu, Q., Altieri, D. C., Murphy, M. E., Shay, J. W.*, et al.* (2018). Exploiting TERT dependency as a therapeutic strategy for NRAS-mutant melanoma. Oncogene *37*, 4058-4072.

Romano, G., Chen, P. L., Song, P., McQuade, J. L., Liang, R. J., Liu, M., Roh, W., Duose, D. Y., Carapeto, F. C. L., Li, J.*, et al.* (2018). A Preexisting Rare PIK3CA(E545K) Subpopulation Confers Clinical Resistance to MEK plus CDK4/6 Inhibition in NRAS Melanoma and Is Dependent on S6K1 Signaling. Cancer Discov *8*, 556-567.

Schmitt, M., Dehay, B., Bezard, E., and Garcia-Ladona, F. J. (2017). U18666A, an activator of sterol regulatory element binding protein pathway, modulates presynaptic dopaminergic phenotype of SH-SY5Y neuroblastoma cells. Synapse *71*.

Seiler, A., Schneider, M., Forster, H., Roth, S., Wirth, E. K., Culmsee, C., Plesnila, N., Kremmer, E., Radmark, O., Wurst, W.*, et al.* (2008). Glutathione peroxidase 4 senses and translates oxidative stress into 12/15-lipoxygenase dependent- and AIF-mediated cell death. Cell Metab *8*, 237-248.

Sengupta, A., Lichti, U. F., Carlson, B. A., Cataisson, C., Ryscavage, A. O., Mikulec, C., Conrad, M., Fischer, S. M., Hatfield, D. L., and Yuspa, S. H. (2013). Targeted disruption of glutathione peroxidase 4 in mouse skin epithelial cells impairs postnatal hair follicle morphogenesis that is partially rescued through inhibition of COX-2. J Invest Dermatol *133*, 1731-1741.

Shi, X., Li, J., Zou, X., Greggain, J., Rodkaer, S. V., Faergeman, N. J., Liang, B., and Watts, J. L. (2013). Regulation of lipid droplet size and phospholipid composition by stearoyl-CoA desaturase. J Lipid Res *54*, 2504-2514.

Shima, H., Pende, M., Chen, Y., Fumagalli, S., Thomas, G., and Kozma, S. C. (1998). Disruption of the p70(s6k)/p85(s6k) gene reveals a small mouse phenotype and a new functional S6 kinase. EMBO J *17*, 6649-6659.

Shimada, K., Skouta, R., Kaplan, A., Yang, W. S., Hayano, M., Dixon, S. J., Brown, L. M., Valenzuela, C. A., Wolpaw, A. J., and Stockwell, B. R. (2016). Global survey of cell death mechanisms reveals metabolic regulation of ferroptosis. Nat Chem Biol.

Skouta, R., Dixon, S. J., Wang, J., Dunn, D. E., Orman, M., Shimada, K., Rosenberg, P. A., Lo, D. C., Weinberg, J. M., Linkermann, A., and Stockwell, B. R. (2014). Ferrostatins inhibit oxidative lipid damage and cell death in diverse disease models. J Am Chem Soc *136*, 4551-4556.

Song, X., Liu, J., Kuang, F., Chen, X., Zeh, H. J., 3rd, Kang, R., Kroemer, G., Xie, Y., and Tang, D. (2021). PDK4 dictates metabolic resistance to ferroptosis by suppressing pyruvate oxidation and fatty acid synthesis. Cell Rep *34*, 108767.

Sridharan, S., and Basu, A. (2020a). Distinct Roles of mTOR Targets S6K1 and S6K2 in Breast Cancer. International Journal of Molecular Sciences *21*.

Sridharan, S., and Basu, A. (2020b). Distinct Roles of mTOR Targets S6K1 and S6K2 in Breast Cancer. Int J Mol Sci *21*.

Sullivan, R. J., Infante, J. R., Janku, F., Wong, D. J. L., Sosman, J. A., Keedy, V., Patel, M. R., Shapiro, G. I., Mier, J. W., Tolcher, A. W.*, et al.* (2018). First-in-Class ERK1/2 Inhibitor Ulixertinib (BVD-523) in Patients with MAPK Mutant Advanced Solid Tumors: Results of a Phase I Dose-Escalation and Expansion Study. Cancer Discov *8*, 184-195.

Takeuchi, K., and Reue, K. (2009). Biochemistry, physiology, and genetics of GPAT, AGPAT, and lipin enzymes in triglyceride synthesis. Am J Physiol Endocrinol Metab *296*, E1195-1209.

Talebi, A., Dehairs, J., Rambow, F., Rogiers, A., Nittner, D., Derua, R., Vanderhoydonc, F., Duarte, J. A. G., Bosisio, F., Van den Eynde, K.*, et al.* (2018). Sustained SREBP-1-dependent lipogenesis as a key mediator of resistance to BRAF-targeted therapy. Nat Commun *9*, 2500.

Teh, J. L. F., Cheng, P. F., Purwin, T. J., Nikbakht, N., Patel, P., Chervoneva, I., Ertel, A., Fortina, P. M., Kleiber, I., HooKim, K.*, et al.* (2018). In Vivo E2F Reporting Reveals Efficacious Schedules of MEK1/2-CDK4/6 Targeting and mTOR-S6 Resistance Mechanisms. Cancer Discov *8*, 568-581.

Tibes, R., Qiu, Y., Lu, Y., Hennessy, B., Andreeff, M., Mills, G. B., and Kornblau, S. M. (2006). Reverse phase protein array: validation of a novel proteomic technology and utility for analysis of primary leukemia specimens and hematopoietic stem cells. Mol Cancer Ther *5*, 2512-2521.

Tolcher, A., Goldman, J., Patnaik, A., Papadopoulos, K. P., Westwood, P., Kelly, C. S., Bumgardner, W., Sams, L., Geeganage, S., Wang, T.*, et al.* (2014). A phase I trial of LY2584702 tosylate, a p70 S6 kinase inhibitor, in patients with advanced solid tumours. Eur J Cancer *50*, 867-875.

Tolcher, A. W., Patnaik, A., Papadopoulos, K. P., Rasco, D. W., Becerra, C. R., Allred, A. J., Orford, K., Aktan, G., Ferron-Brady, G., Ibrahim, N.*, et al.* (2015). Phase I study of the

MEK inhibitor trametinib in combination with the AKT inhibitor afuresertib in patients with solid tumors and multiple myeloma. Cancer Chemother Pharmacol *75*, 183-189.

Tsoi, J., Robert, L., Paraiso, K., Galvan, C., Sheu, K. M., Lay, J., Wong, D. J. L., Atefi, M., Shirazi, R., Wang, X.*, et al.* (2018). Multi-stage Differentiation Defines Melanoma Subtypes with Differential Vulnerability to Drug-Induced Iron-Dependent Oxidative Stress. Cancer Cell.

Tyanova, S., Temu, T., Sinitcyn, P., Carlson, A., Hein, M. Y., Geiger, T., Mann, M., and Cox, J. (2016). The Perseus computational platform for comprehensive analysis of (prote)omics data. Nat Methods *13*, 731-740.

Villanueva, J., Infante, J. R., Krepler, C., Reyes-Uribe, P., Samanta, M., Chen, H. Y., Li, B., Swoboda, R. K., Wilson, M., Vultur, A.*, et al.* (2013). Concurrent MEK2 mutation and BRAF amplification confer resistance to BRAF and MEK inhibitors in melanoma. Cell Rep *4*, 1090-1099.

Viswanathan, V. S., Ryan, M. J., Dhruv, H. D., Gill, S., Eichhoff, O. M., Seashore-Ludlow, B., Kaffenberger, S. D., Eaton, J. K., Shimada, K., Aguirre, A. J.*, et al.* (2017). Dependency of a therapy-resistant state of cancer cells on a lipid peroxidase pathway. Nature *547*, 453-457.

Vu, H. L., and Aplin, A. E. (2016). Targeting mutant NRAS signaling pathways in melanoma. Pharmacol Res *107*, 111-116.

Wang, B. T., Ducker, G. S., Barczak, A. J., Barbeau, R., Erle, D. J., and Shokat, K. M. (2011). The mammalian target of rapamycin regulates cholesterol biosynthetic gene expression and exhibits a rapamycin-resistant transcriptional profile. Proc Natl Acad Sci U S A *108*, 15201-15206.

Wang, C. C., and Janes, K. A. (2014). Non-genetic heterogeneity caused by differential single-cell adhesion. Cell Cycle *13*, 2149-2150.

Williams, K. J., Argus, J. P., Zhu, Y., Wilks, M. Q., Marbois, B. N., York, A. G., Kidani, Y., Pourzia, A. L., Akhavan, D., Lisiero, D. N.*, et al.* (2013). An essential requirement for the SCAP/SREBP signaling axis to protect cancer cells from lipotoxicity. Cancer Res *73*, 2850-2862.

Willson, T. M., Brown, P. J., Sternbach, D. D., and Henke, B. R. (2000). The PPARs: from orphan receptors to drug discovery. J Med Chem *43*, 527-550.

Xu, H. E., Lambert, M. H., Montana, V. G., Parks, D. J., Blanchard, S. G., Brown, P. J., Sternbach, D. D., Lehmann, J. M., Wisely, G. B., Willson, T. M.*, et al.* (1999). Molecular recognition of fatty acids by peroxisome proliferator-activated receptors. Mol Cell *3*, 397-403.

Yang, W. S., SriRamaratnam, R., Welsch, M. E., Shimada, K., Skouta, R., Viswanathan, V. S., Cheah, J. H., Clemons, P. A., Shamji, A. F., Clish, C. B.*, et al.* (2014). Regulation of ferroptotic cancer cell death by GPX4. Cell *156*, 317-331.

Yi, J., Zhu, J., Wu, J., Thompson, C. B., and Jiang, X. (2020). Oncogenic activation of PI3K-AKT-mTOR signaling suppresses ferroptosis via SREBP-mediated lipogenesis. Proc Natl Acad Sci U S A *117*, 31189-31197.

Figure 1. S6K2 is a vulnerability in NRAS-mutant melanoma resistant to MAPK inhibitors

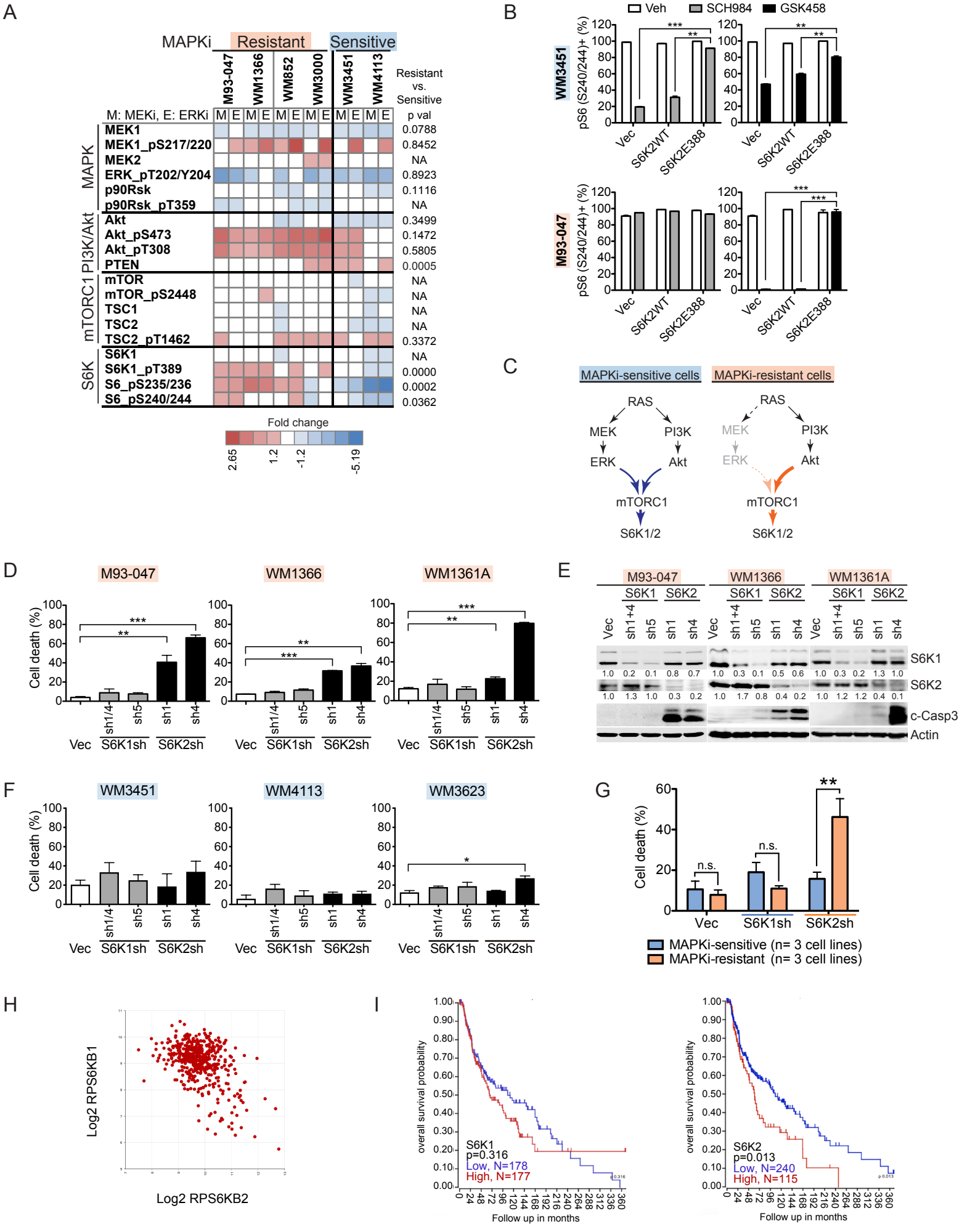

Figure 2. Depletion of S6K2 triggers lipid peroxidation facilitating cell death

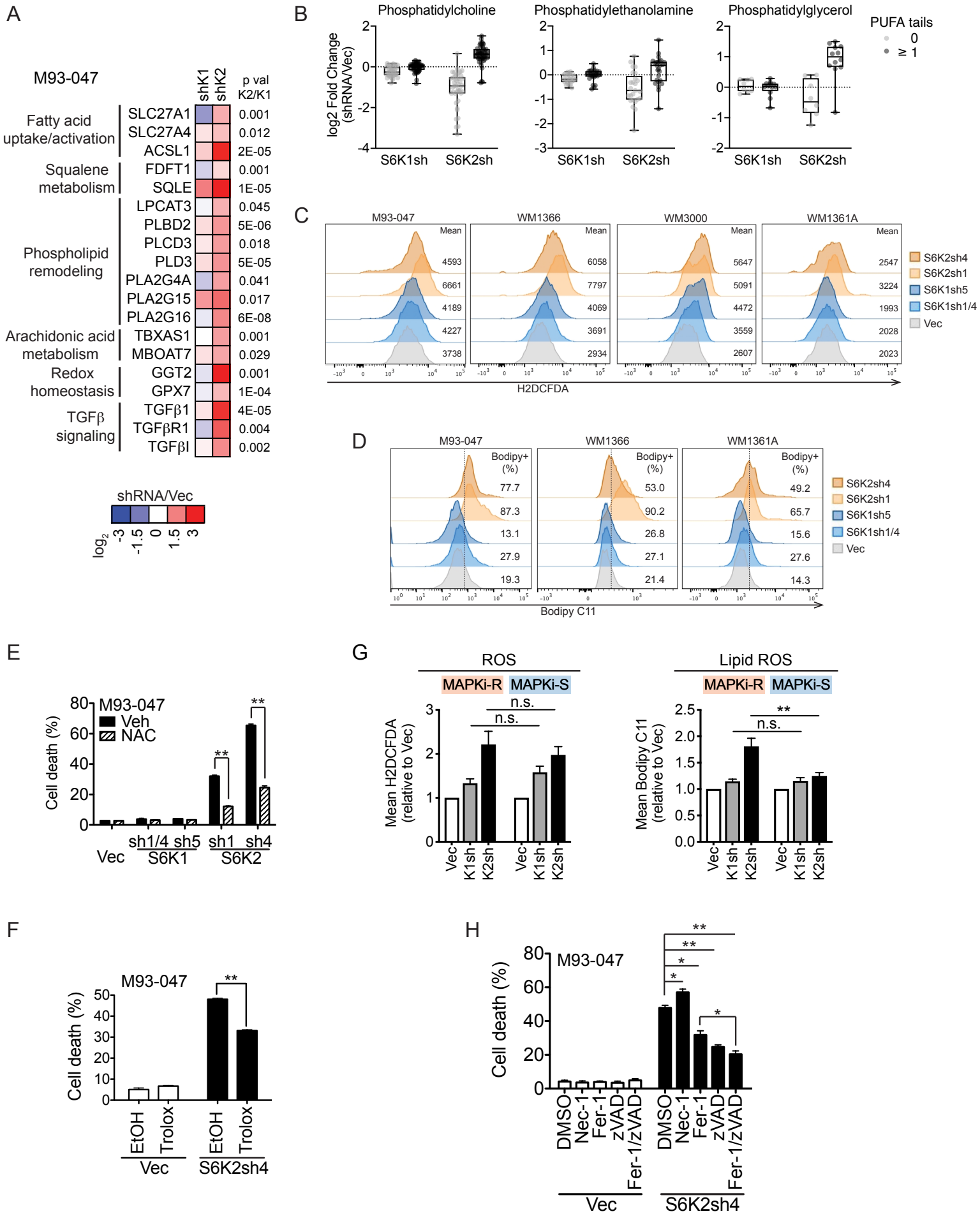

Figure 3. S6K1 and SREBPs contribute to oxidative cell death

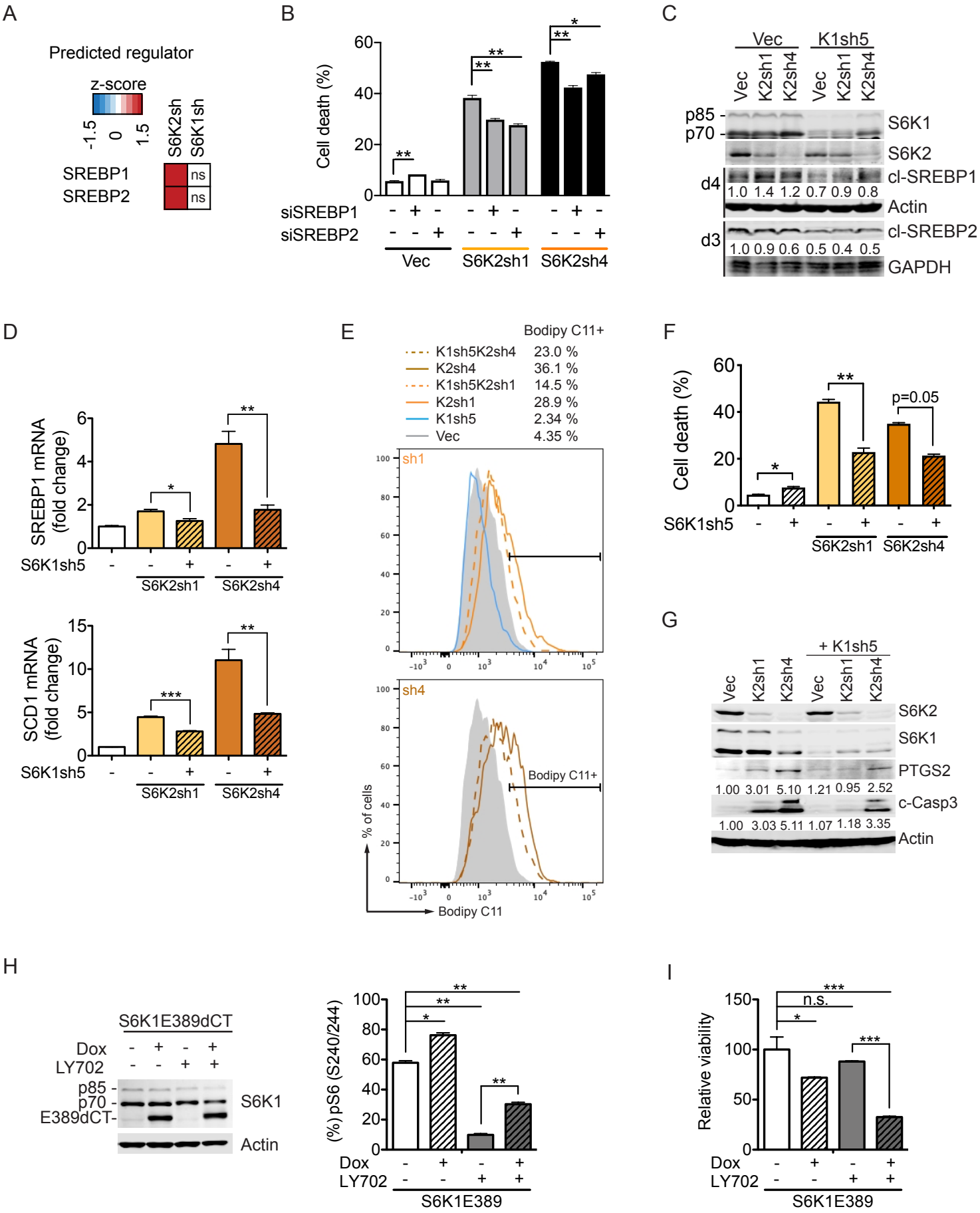

Figure 4. Suppression of S6K2 relieves negative regulation on PPARα facilitating lipid peroxidation

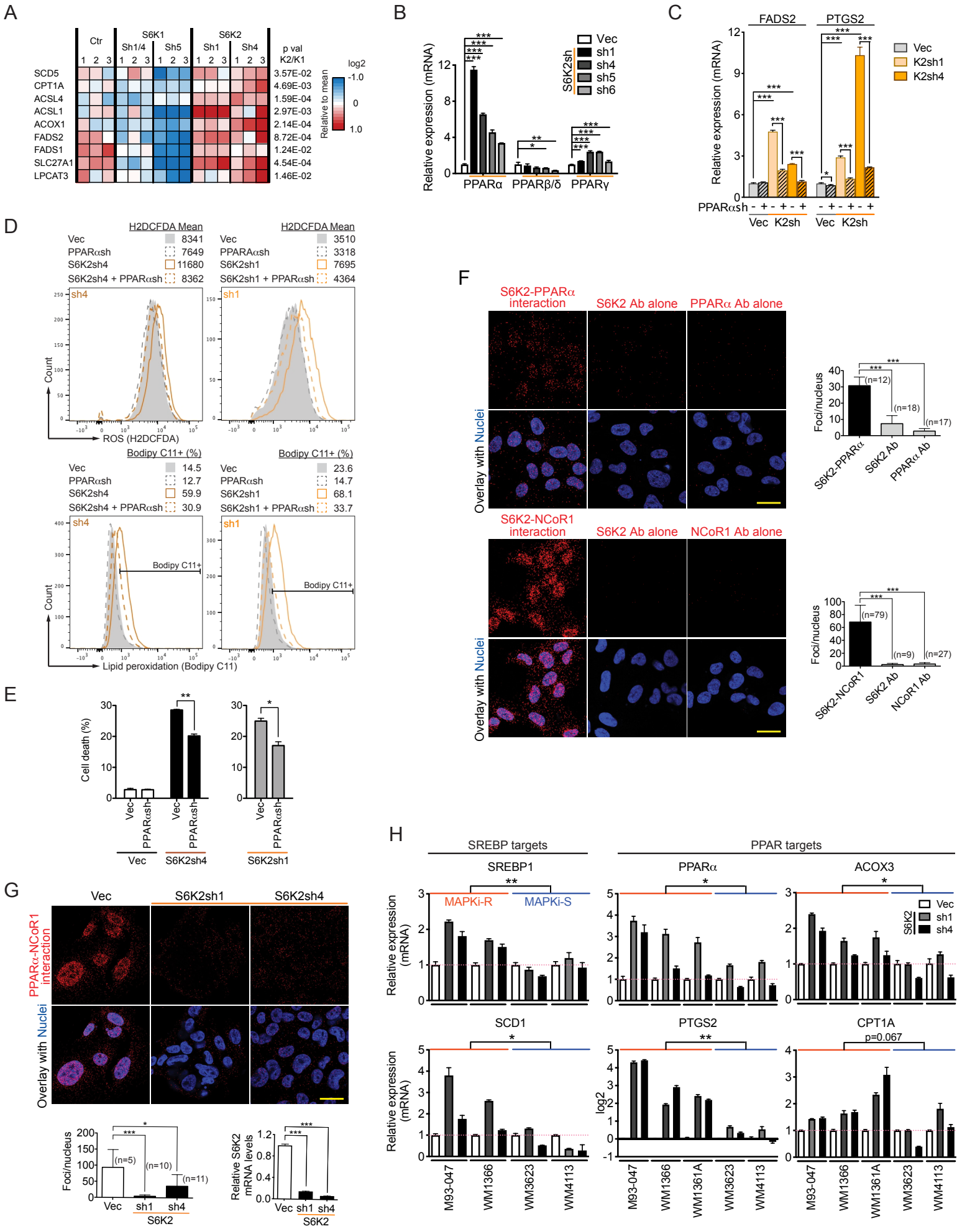

Figure 5. PUFAs potentiate the oxidative cell death inducing effect of PPARα agonists

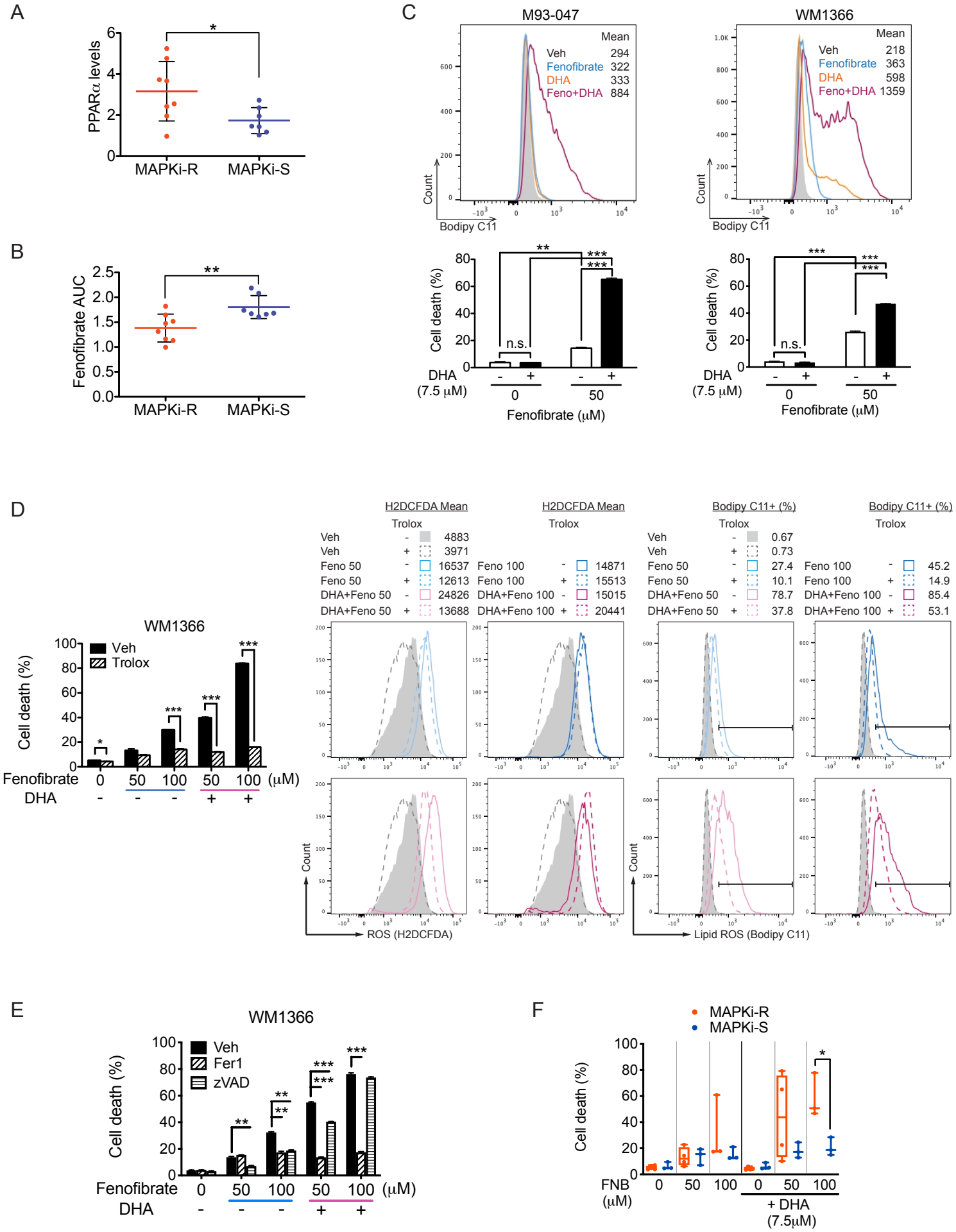

Figure 6. MAPKi-resistant NRAS-mutant melanoma is sensitive to combination of PPARα agonists and PUFA

A

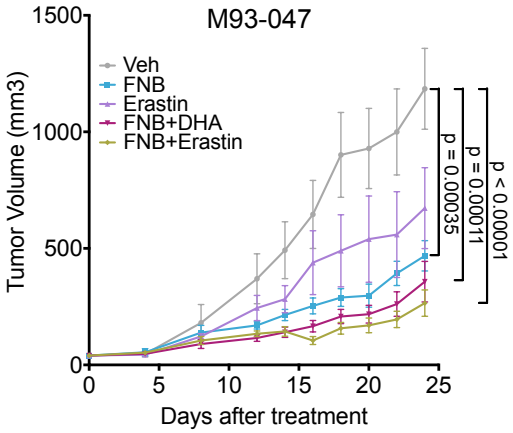

D

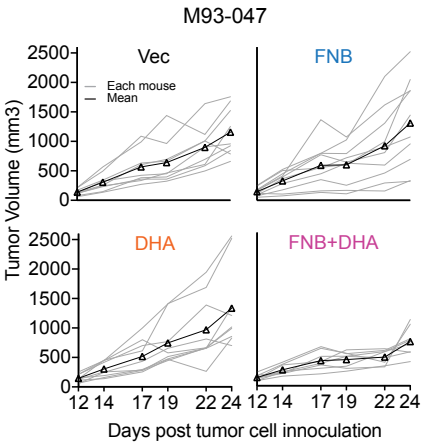

Treatment group comparison		p values	FDR adjusted p values
Veh vs.	*FNB*	0.7134	0.8193
	DHA	0.5115	0.7672
	FNB+DHA	0.0012	0.0072
FNB vs.	*DHA*	0.8193	0.8193
	FNB+DHA	0.0338	0.0677
DHA vs.	*FNB+DHA*	0.0141	0.0422

E

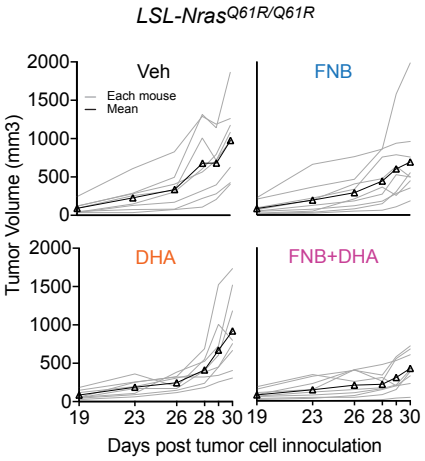

Treatment group comparison		p values	FDR adjusted p values
Veh vs.	*FNB*	0.2898	0.4348
	DHA	0.7032	0.7032
	FNB+DHA	0.0016	0.0096
FNB vs.	*DHA*	0.5155	0.6186
	FNB+DHA	0.0441	0.0882
DHA vs.	*FNB+DHA*	0.0108	0.0324

B

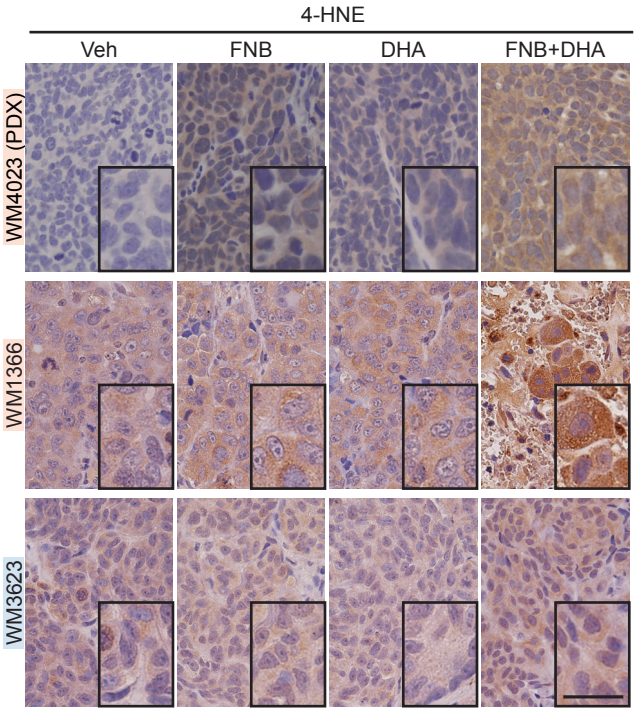

F

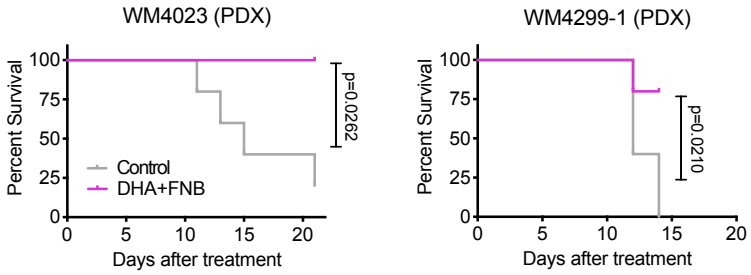

C

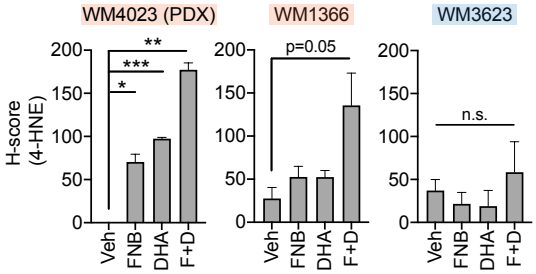

G

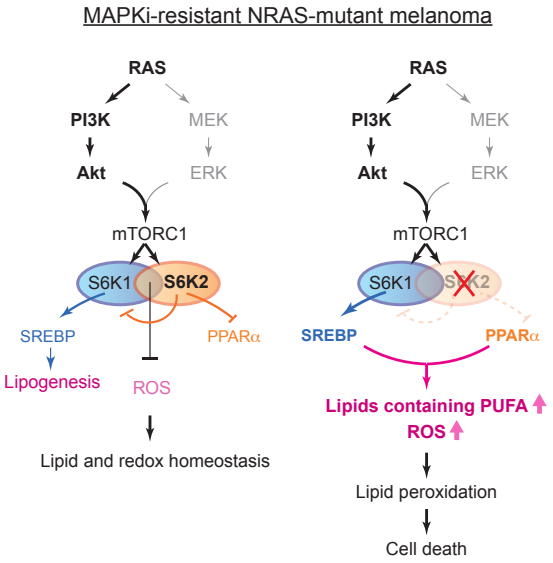

Figure S1 (1 of 2). Related to Figure 1. MAPK and PI3K/mTOR differentially regulate S6K in NRAS-mutant melanoma cells sensitive vs. resistant to MAPK inhibitors

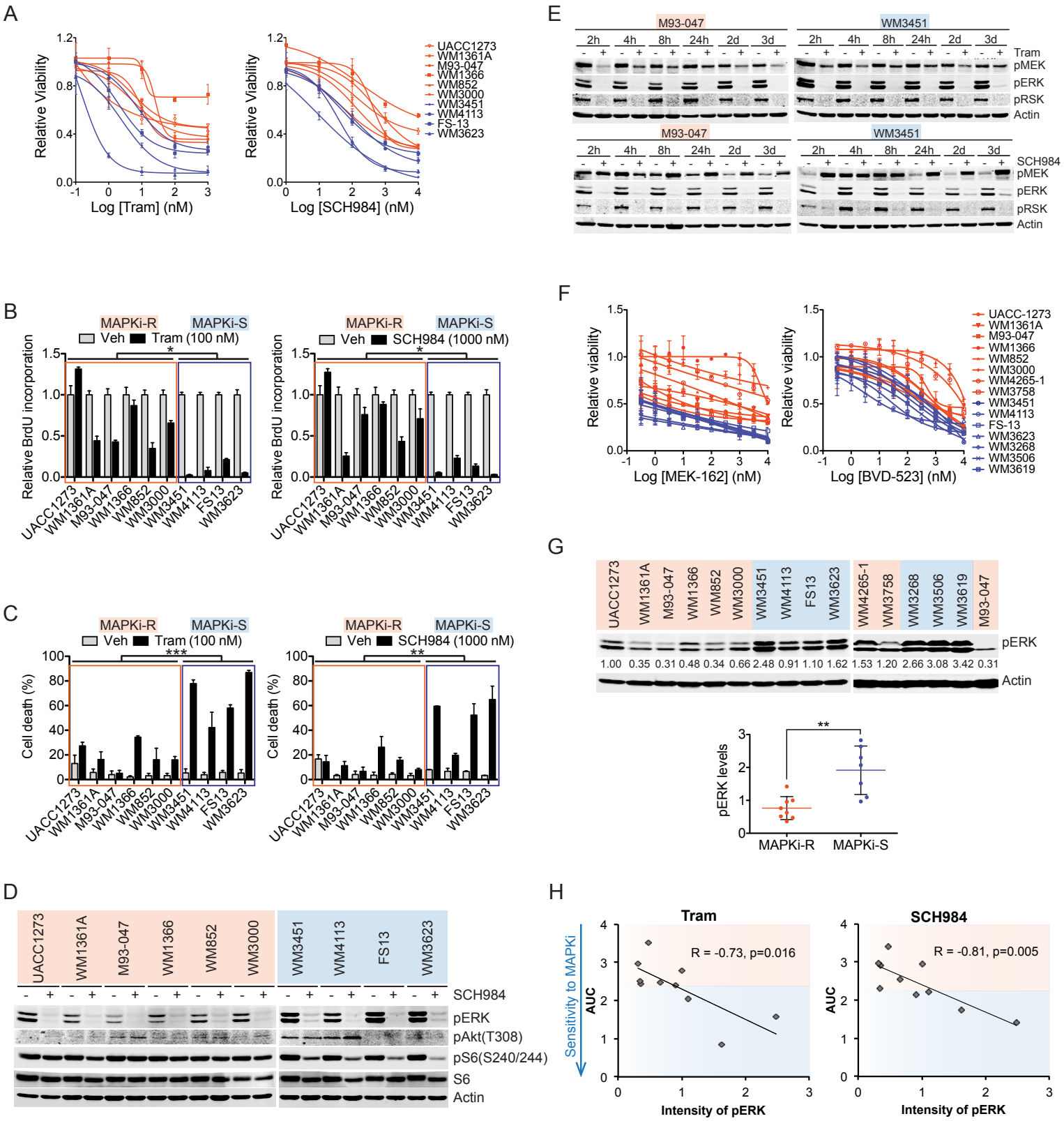

Figure S1 (2 of 2). Related to Figure 1. MAPK and PI3K/mTOR differentially regulate S6K in NRAS-mutant melanoma cells sensitive vs. resistant to MAPK inhibitors

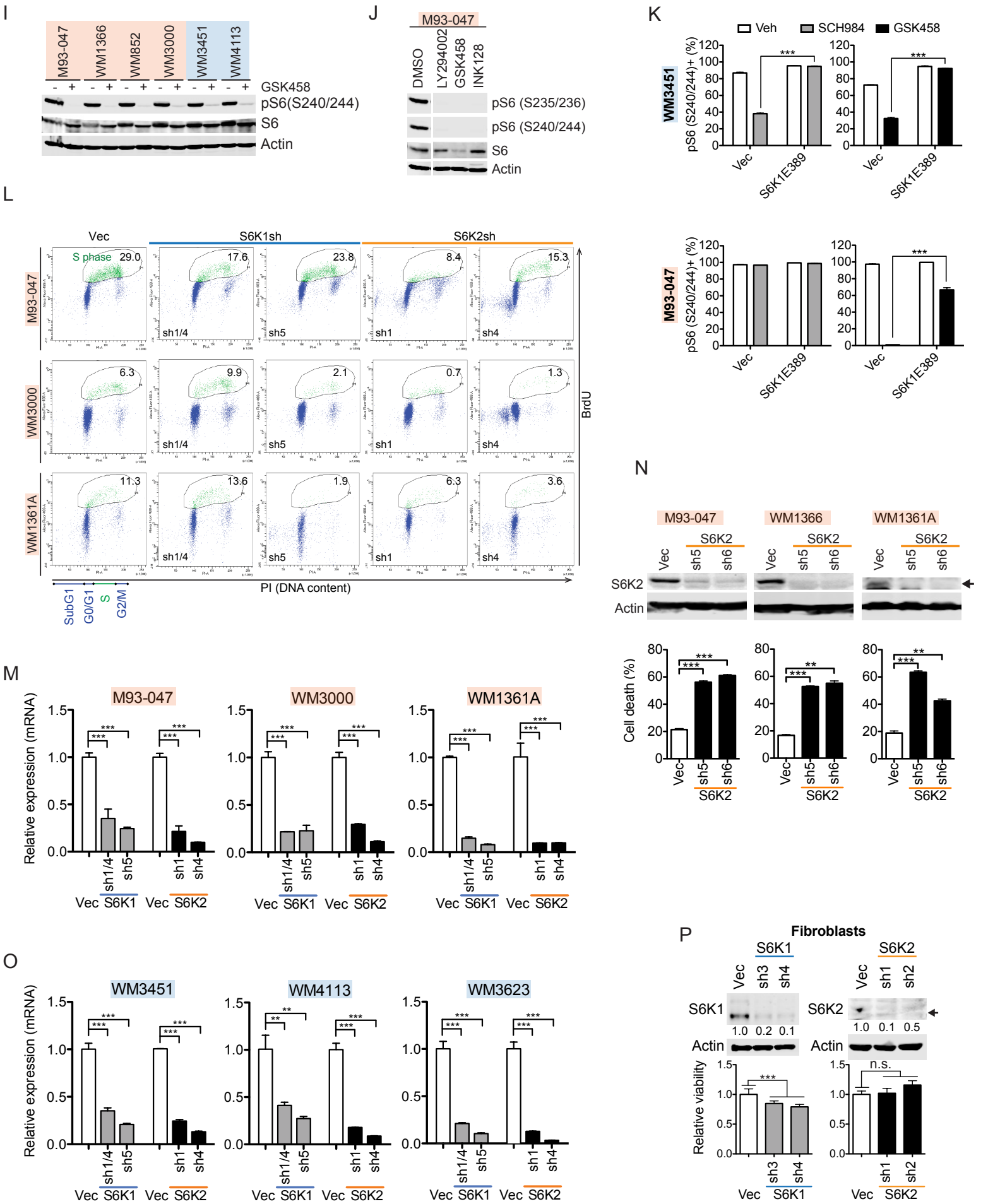

Figure S2 (1 of 2). Related to Figure 2. Depletion of S6K2 perturbs lipid metabolism and leads to widespread oxidative damage and cell death.

A

M93-047

Proteomics

Top proteins affected by S6K2sh but not S6K1sh

Sorted by fold change, p-value

S6K2sh vs. Vec < 0.05 and S6K1sh vs. Vec > 0.05

Gene names	S6K2sh vs. Vec Fold change	S6K2sh vs. Vec p-value
GGT2	41.56	0.0188
COL4A1	22.21	0.0012
SLC14A1	14.15	0.0280
HHIP	11.77	0.0029
SELS	11.61	0.0083
TMEM106B	10.58	0.0010
GMIP	10.15	0.0302
COL15A1	8.72	0.0020
SQLE	8.39	0.0037
LAMB2	8.31	0.0004
GRAMD3	8.20	0.0004
RBBP6	7.92	0.0169
GBP4	6.91	0.0043
ACSL1	6.75	0.0196
KIAA1217	6.49	0.0040
USP36	6.15	0.0045
TGFB1	5.76	0.0001
NOM1	5.70	0.0075
TBC1D8B	5.70	0.0071
ITGA1	5.70	0.0140
MBLAC2	5.48	0.0083
ARL5B	5.47	0.0079
CLU	5.25	0.0015
COL11A1	5.09	0.0014
ITGA9	5.03	0.0027
FGF2	5.01	0.0011
SLC30A9	4.91	0.0025
GDPD1	4.73	0.0001
ARHGAP26	4.48	0.0003
DHCR7	4.41	0.0011
ABAT	4.30	0.0000
RNASET2	4.17	0.0038
PBXIP1	4.05	0.0014
CPXM1	4.05	0.0048
RAB7L1	3.93	0.0001
CTHRC1	3.89	0.0022
SOD2	3.88	0.0002
PTEN2	3.83	0.0006
COL7A1	3.33	0.0002
RHBDD2	3.31	0.0007
ALDH1A3	2.63	0.0000
RPL22L1	-3.20	0.0002
IQGAP3	-3.57	0.0019
SMG7	-4.16	0.0025
HIRIP3	-4.19	0.0034
HYPK	-4.25	0.0016
CDCA5	-4.44	0.0017
DLGAP5	-4.98	0.0213
CDCA8	-5.92	0.0018
ATAD5	-6.18	0.0037
RPS6KB2	-6.32	0.0292
GINS1	-6.38	0.0013
KIFC3	-6.88	0.0304
PDLIM2	-7.30	0.0106
RPL36AL	-8.29	0.0168
TBC1D2B	-8.82	0.0066
ARGLU1	-12.35	0.0192
PDE8A	-18.90	0.0097

- Lipid metabolism
- Stress response, inflammation
- Cell cycle
- Redox homeostasis/Glutathione metabolism
- Angiogenesis
- Autophagy/lysosome
- TGFβ signaling

GGT2	Eicosanoid signaling
SQLE	Lipid synthesis
ACSL1	Fatty acid activation, lipid synthesis, fatty acid degradation
CLU	Lipid transport, membrane recycling
GDPD1	Glycerophospholipid catabolism
DHCR7	Lipid synthesis
ALDH1A3	Detoxifying aldehydes generated by lipid peroxidation

IPA canonical pathways

- Phospholipases
- Eicosanoid signaling
- Atherosclerosis signaling
- Cholesterol biosynthesis
- Zymosterol biosynthesis
- Stearate Biosynthesis I
- Cell cycle control of chromosomal replication
- Hepatic fibrosis/hepatic stellate cell activation
- G6P signaling pathways
- Inhibition of angiogenesis by TSP1
- Pyrimidine deoxyribonucleotides de novo biosynthesis I
- dTMP de novo biosynthesis
- Chondroitin Sulfate degradation
- p38 MAPK signaing
- Intrinsic prothrombin activation pathway
- Granulocyte Adhesion and diapedesis
- Granzyme A signaling
- Factors promoting cardiogenesis in vertbrates
- Wnt/b-catenin signaling

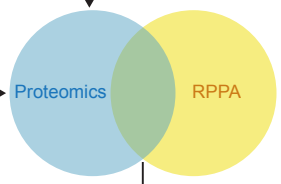

Lipid metabolism & Redox balance

B

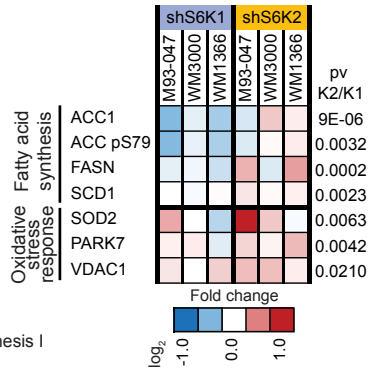

C

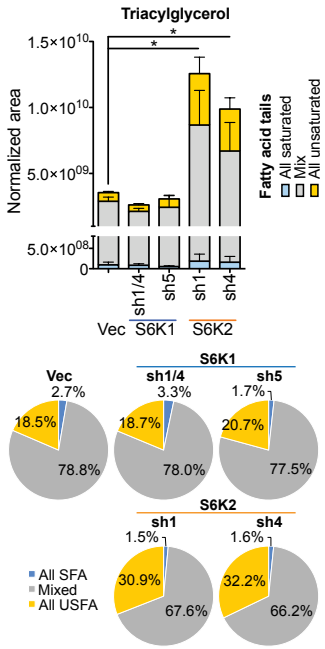

D

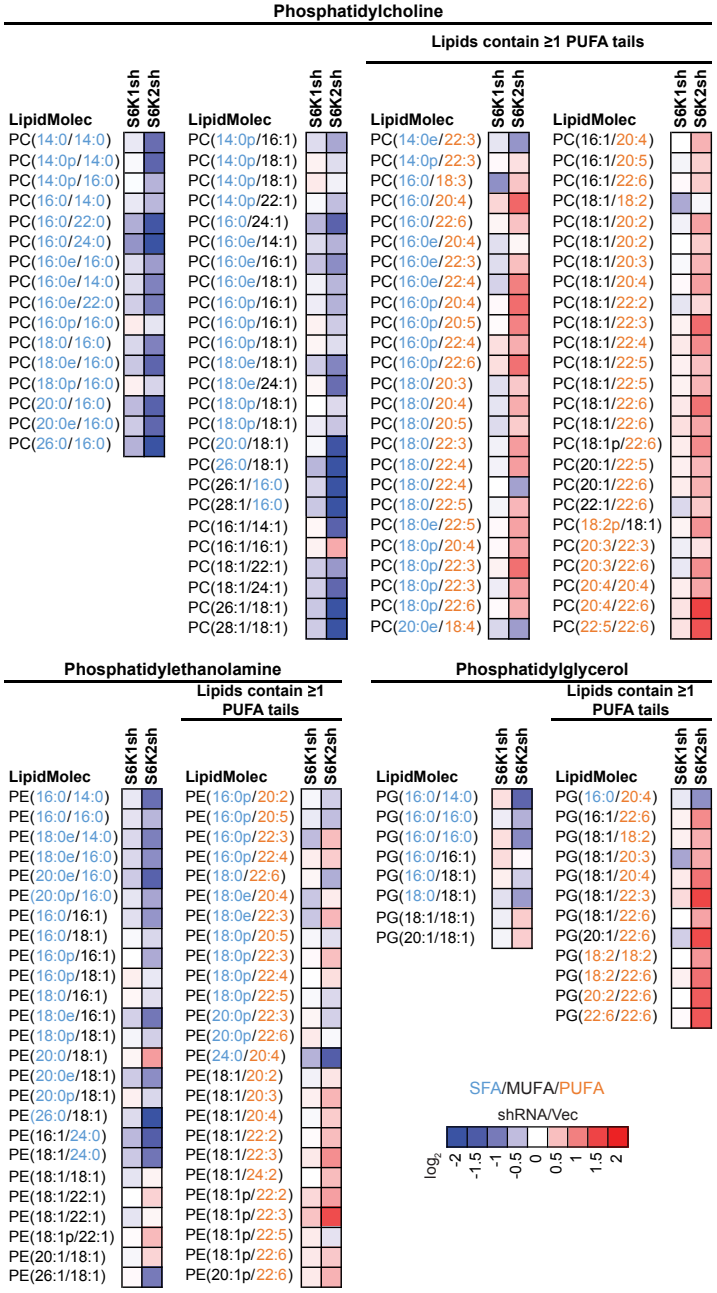

Figure S2 (2 of 2). Related to Figure 2. Depletion of S6K2 perturbs lipid metabolism and leads to widespread oxidative damage and cell death.

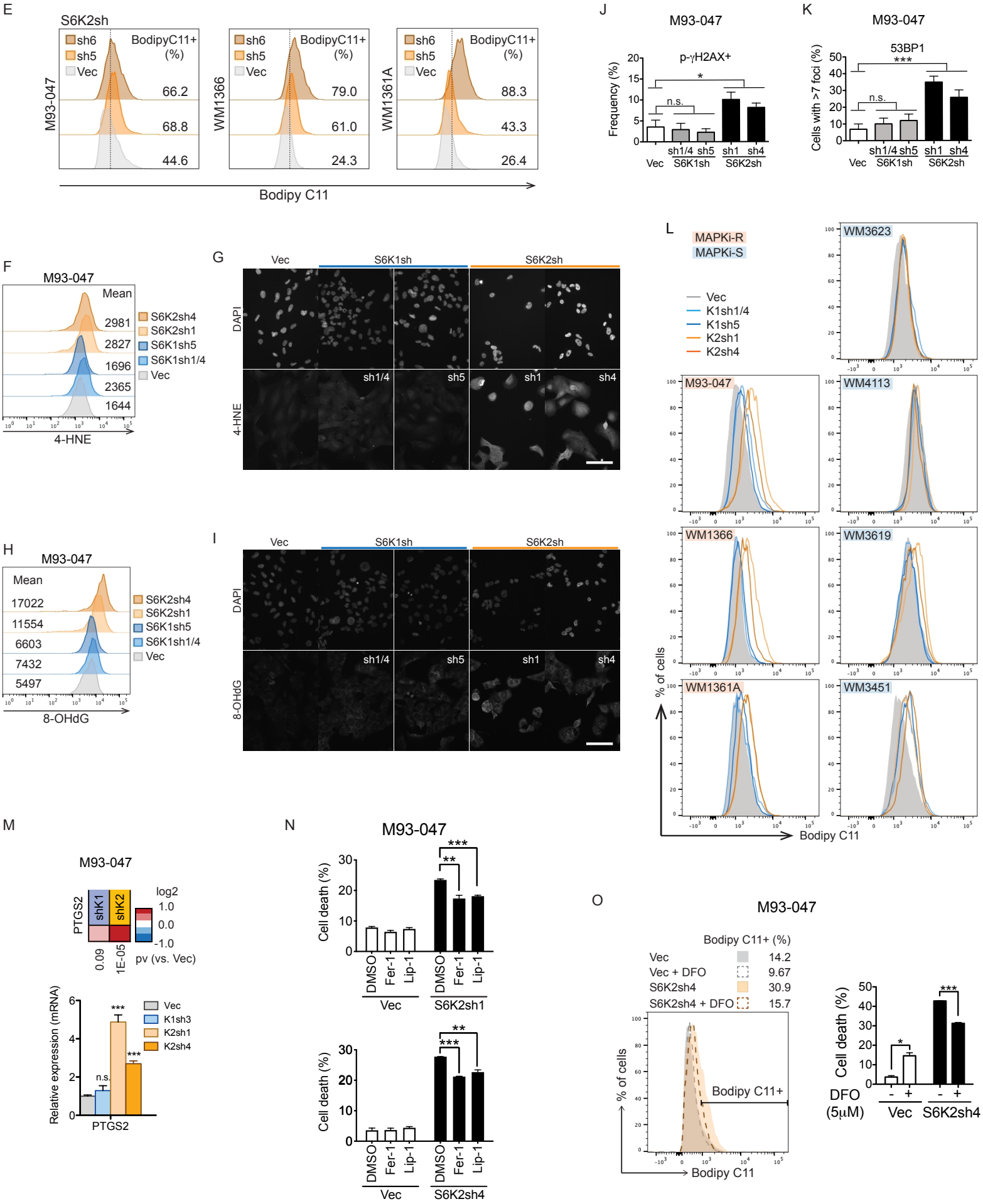

Figure S3 (1 of2). Related to Figure 3. Concomitant suppression of S6K1 diminishes the effects of S6K2 depletion

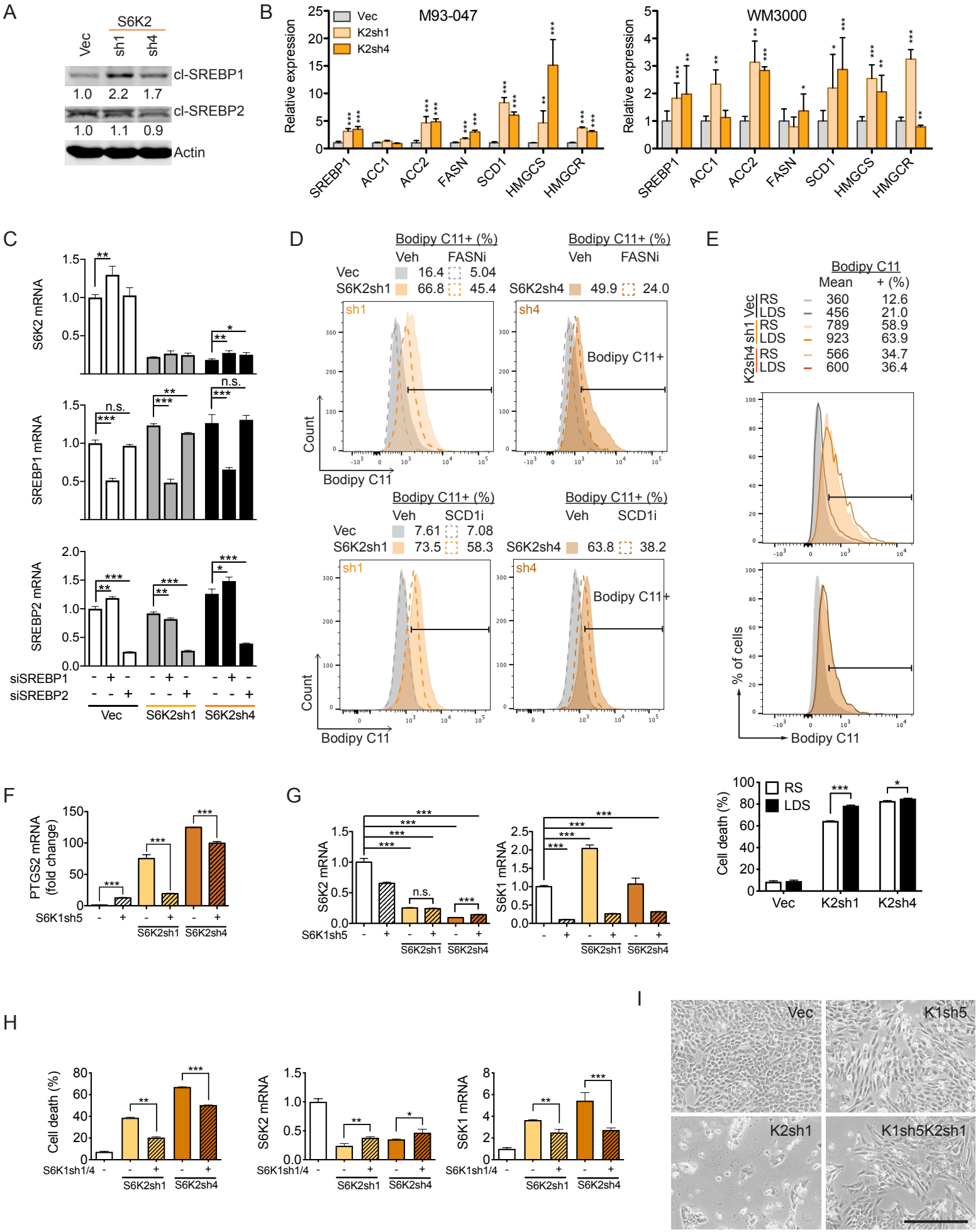

Figure S3 (2 of 2). Related to Figure 3. Concomitant suppression of S6K1 diminishes the effects of S6K2 depletion

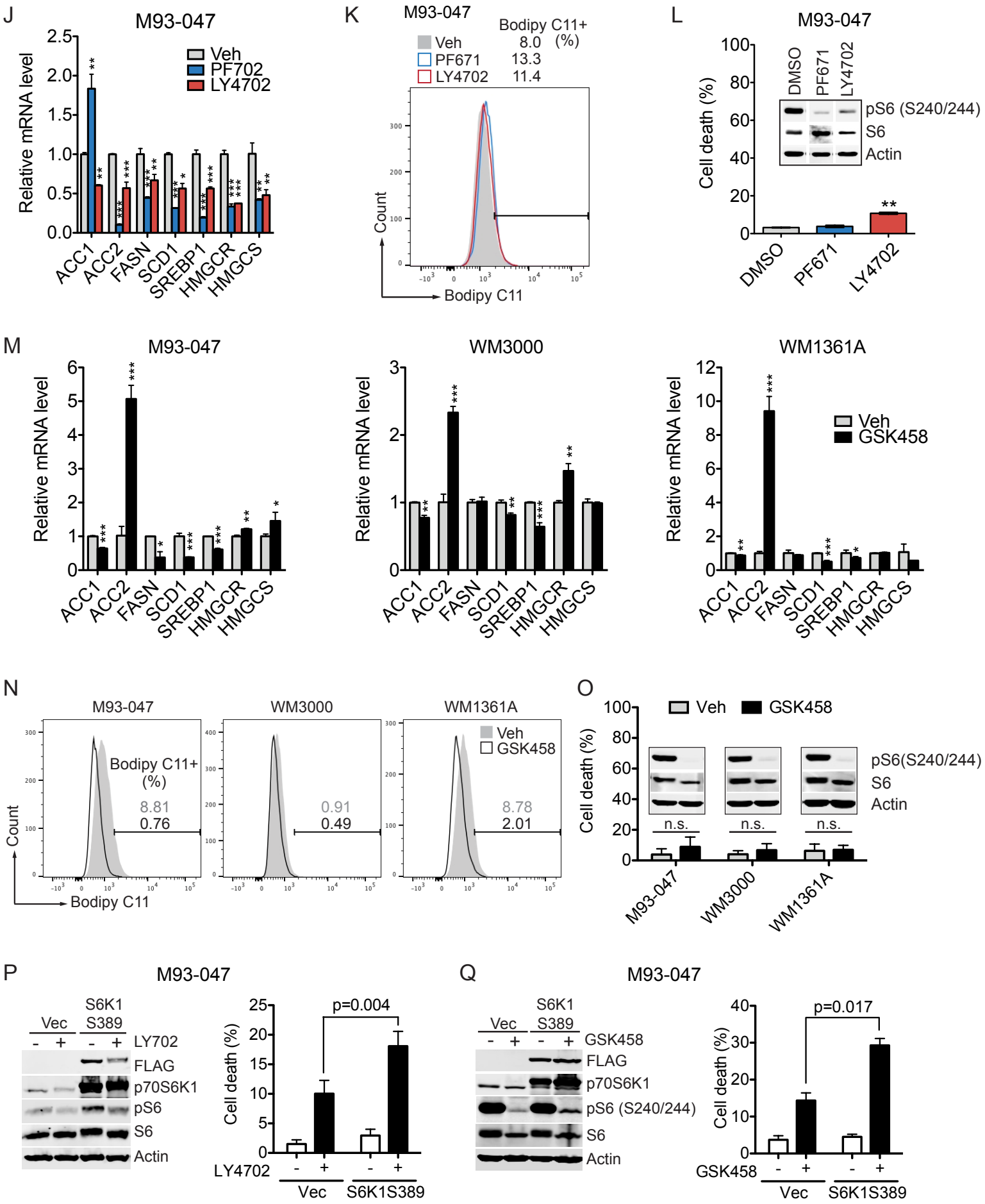

Figure S4. (1 of 2) Related to Figure 4. PPARα facilitates cell death by S6K2 silencing

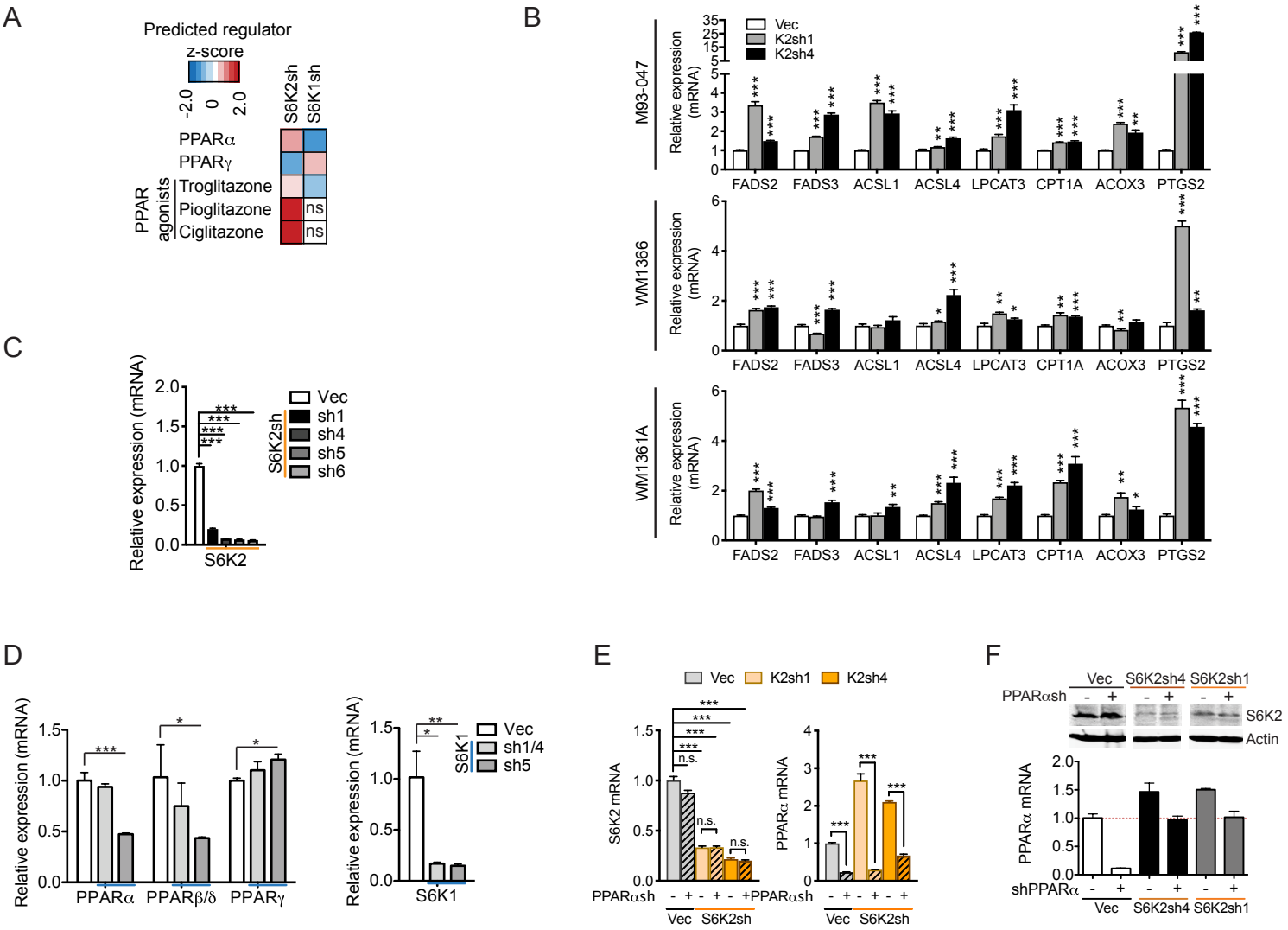

Figure S4. (2 of 2) Related to Figure 4. PPARα facilitates cell death by S6K2 silencing

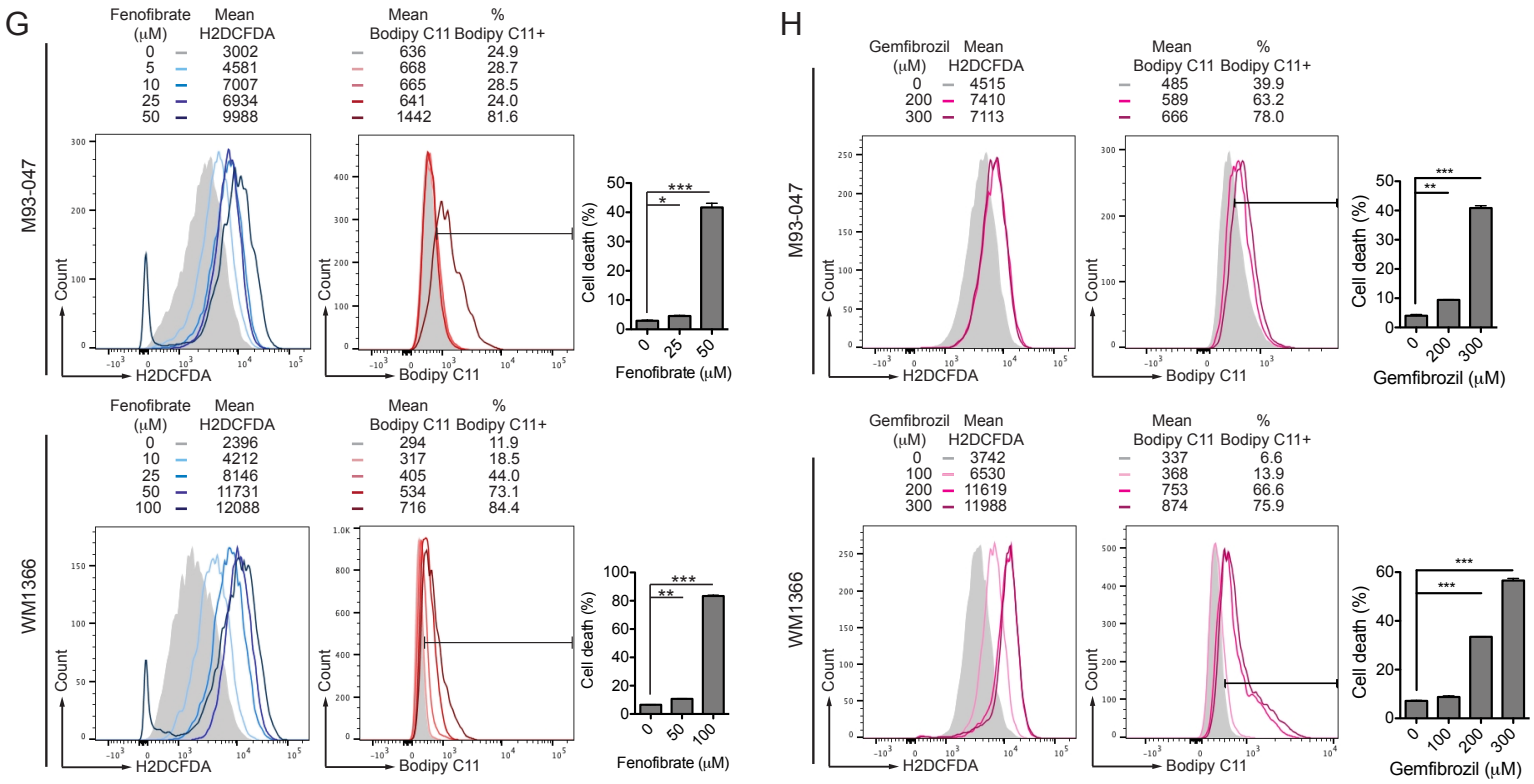

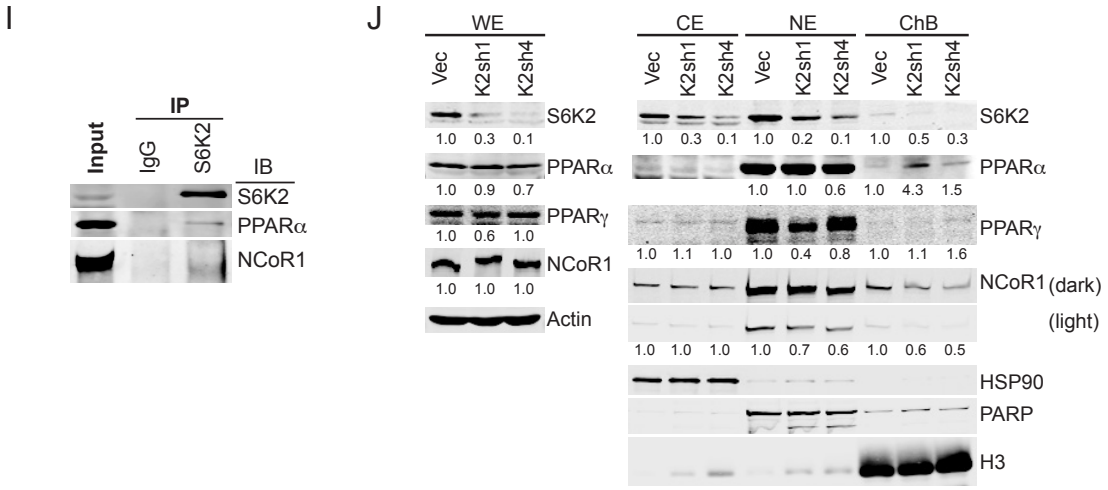

Figure S5. (1 of 2) Related to Figure 5. PPARα agonist and PUFA combination mimics the effects of S6K2 inhibition in NRAS-mutant melanoma resistant to MAPKi

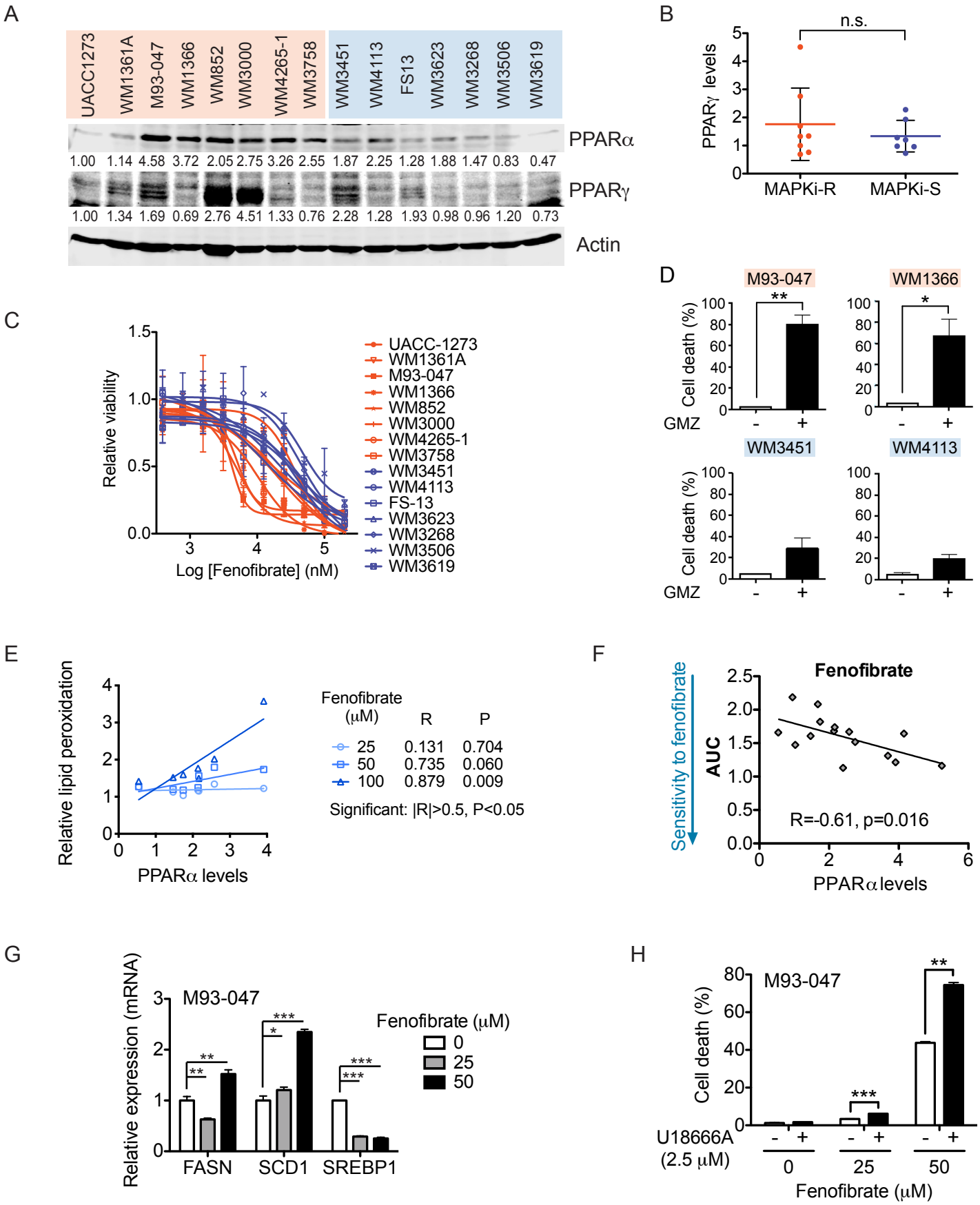

Figure S5. (2 of 2) Related to Figure 5. PPARα agonist and PUFA combination mimics the effects of S6K2 inhibition in NRAS-mutant melanoma resistant to MAPKi

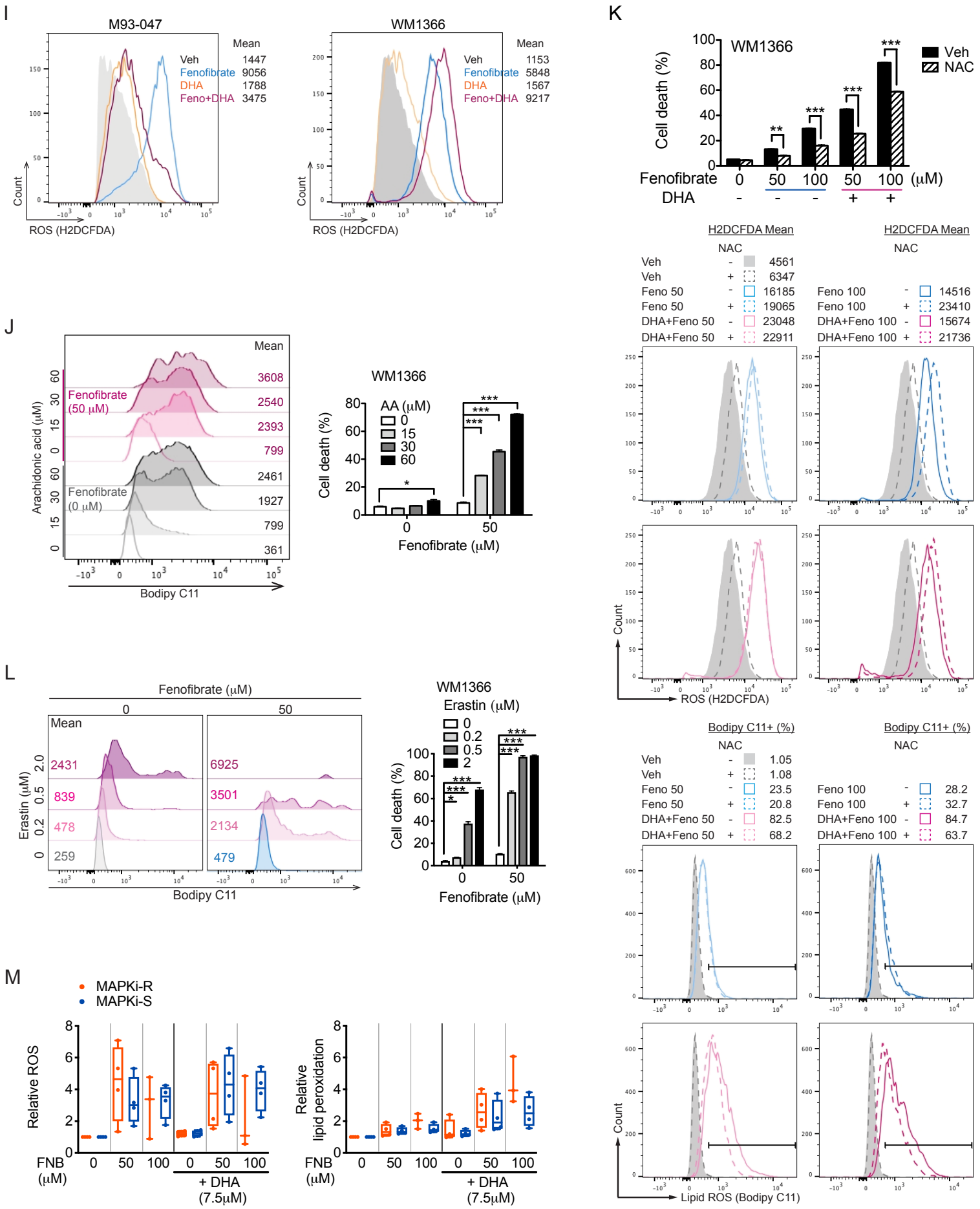
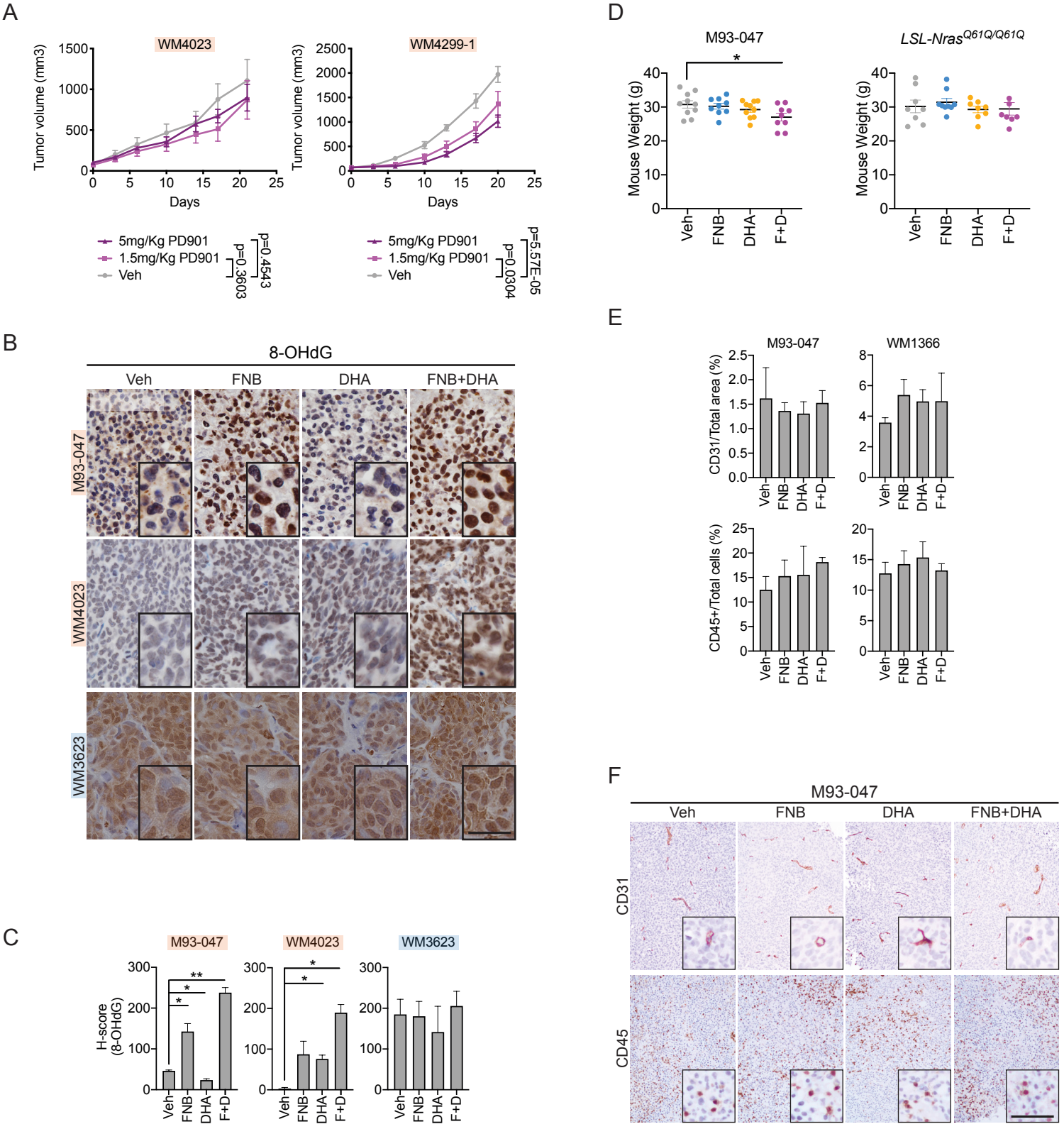
Figure S6. Related to Figure 6. Mimicking the effects of S6K2 suppression restrains NRAS-mutant melanoma resistant to MAPKi